nature geoscience

Article

https://doi.org/10.1038/s41561-024-01378-5

Early Jurassic large igneous province carbon emissions constrained by sedimentary mercury

In the format provided by the authors and unedited

Summary of SI sections:

S1: Hg data analysis & host-phase corrections

S1.1: Hg data used in this study:

i) Data sources:

We compile Hg data for the Mochras core from Percival et al. (2015; 2016)[1,2] and Ruhl et al. (2022)[3] and combine it with our new data to create a composite Hg record which spans ~900 m of stratigraphy from the late Sinemurian through the Toarcian.

ii) Sampling resolution (in time):

The sampling resolution of our record varies. The majority of the record is sampled at 10–40 kyr resolution; however, a few larger gaps exist in the Sinemurian. The median sampling resolution (difference in age between subsequent samples) for the entire record is 21 kyr, whereas for the T-OAE interval it is 12 kyr (Fig. S2). For information about the age model, please see SI Section 3. The sampling resolution was primarily controlled by sample availability, as much material towards the lower section of the core is no longer available.

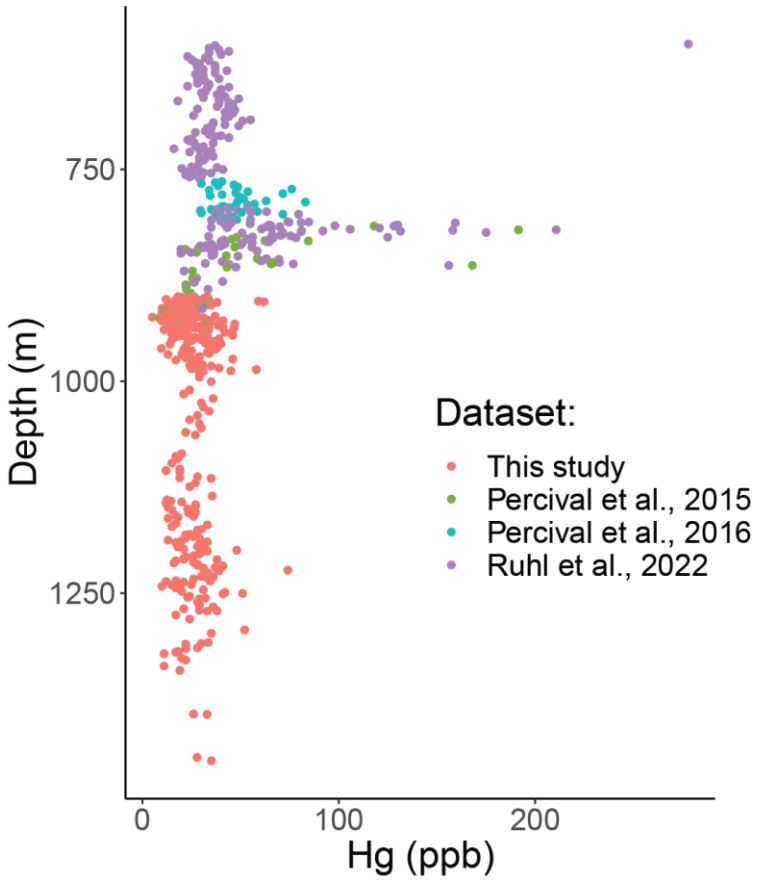

Figure S1: Hg data from the Mochras core; points colored by reference. The orange points, from the ~850 m depth point and below, are new data presented in this study. Individual data points are shown here to show sampling resolution (by depth).

Each interval of interest: the Sinemurian – Pliensbachian boundary, the upper Pliensbachian, and Toarcian, are each sampled at high-resolution (10-20 kyr). The intervals of the record with lower sampling resolution, in particular the lower Sinemurian and, to a lesser extent, the mid-Pliensbachian (191–190 Ma), may be missing significant Hg peaks. For these intervals, our volcanic emissions estimates are a minimum.

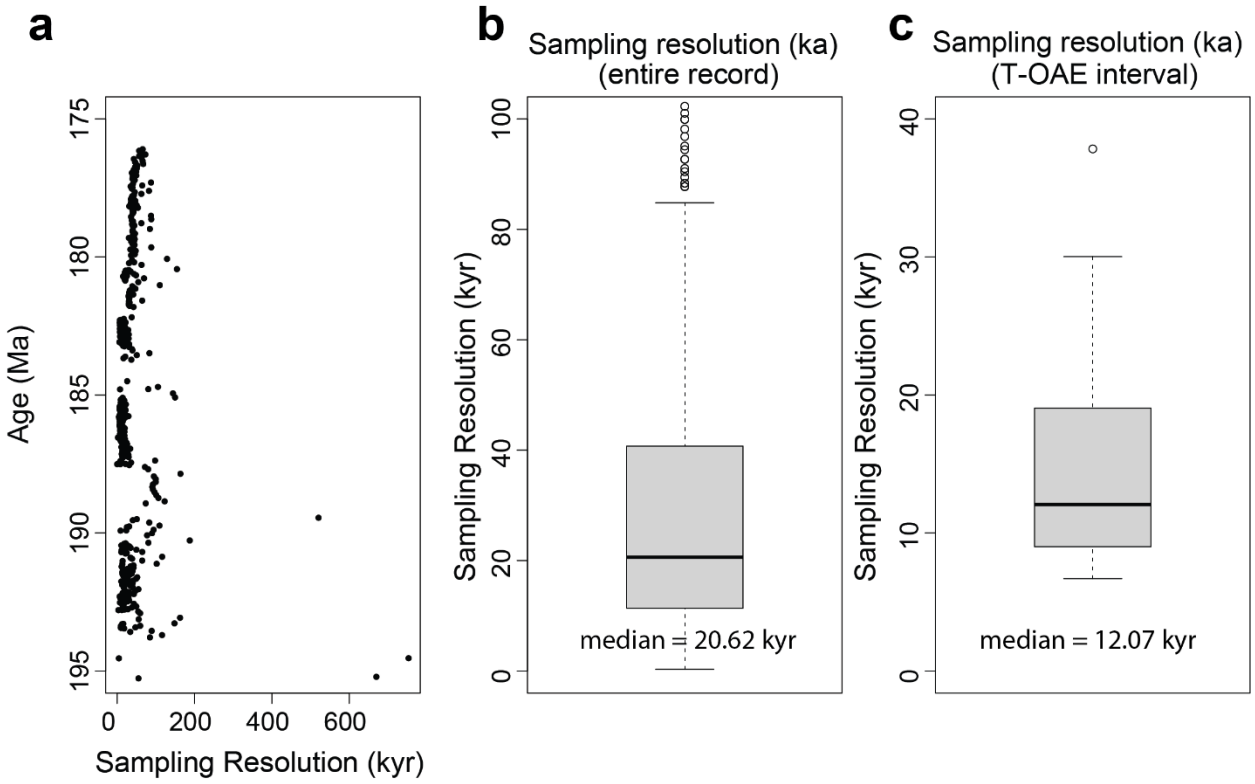

Figure S2: ***a)*** *Sampling resolution (difference in age between adjacent samples)* vs *age (Ma) in the Mochras borehole compiled Hg record.* ***b)*** *Box-whisker-plots (using standard boxplot settings, box bound by 25 and 75 percentiles, and the line is at the 50 percentile (median), the whiskers extend to maximum 1.5 times to interquartile range and outliers are shown as individual points) of sampling resolution values for the entire record (n=555).* ***c)*** *Boxplot of sampling resolution for only the T-OAE portion of the record (182–183 Ma) (n=60). Note the y-axes in panels b and c are scaled differently.*

S1.2: Host-phase corrections:

Our goal is to investigate the changes in Hg deposition through time as a reflection of changing availability of environmental mercury. To do this, we need to account for co-variation between Hg and other geochemical parameters such as TOC, sulfur (S), and clay minerals, which can act as host-phases for mercury in sediments[4,5]. Hg is commonly associated with organic matter in the water column and in sediments deposited throughout geological history[6,7]. To understand how Hg varies independently of concentration of TOC, Hg/TOC is used as a basis for chemostratigraphic study[1,7,8]. However, there are several key limitations of the Hg/TOC proxy, particularly in the case of the Mochras dataset, which affect our aim to quantify the excess Hg in the environment due to volcanic emissions at given points in the record.

In the following sub-sections, we introduce four specific problems that are difficult to address using Hg/TOC, in some cases, and describe the solutions we use for the Mochras dataset: (i) dilution by carbonate, (ii) nonlinear relationships between Hg and host-phases, (iii) multiple potential host-phases, and (iv) a lack of quantification of the actual excess of Hg compared to background. These problems are not unique to the Mochras dataset and have been acknowledged previously to varying degrees[3,4,7]. As a result, we expect our new approach and aspects thereof, despite being perhaps more laborious to apply than simple Hg/TOC normalization, will be useful for other datasets besides the Mochras data presented here – provided that certain conditions are met. We built our approach on a set of explicit and physically/chemically justifiable assumptions, and then developed correction methods that can sequentially address the four problems mentioned above.

In our approach we make two underlying assumptions:

- We assume that if a "correction" is needed to the Hg data it will be apparent due to co-variation between Hg and another variable (e.g., TOC), *within a given dataset.* For example, although Hg and TOC correlate in many cases, if they are not significantly correlated within a specific dataset then it would be inappropriate to apply a correction to TOC in that case. We also generally assume the converse: that if co-variation between Hg and another variable is present, then a correction is needed. This assumption allows for dataset- (and hence locality) specific relationships between Hg and host-phases rather than assuming a broad, generalized relationship. Datasets for Hg in sediments across a variety of environments clearly illustrate that Hg-host-phase speciation is complex[4,6,9] and assuming a general, global relationship might lead to significant errors.
- We assume that the nature of the co-variation within each specific dataset determines the type of correction to be made. For example, if Hg and TOC co-vary nonlinearly, then a correction which takes this nonlinearity into account (i.e., not a linear Hg/TOC correction) needs to be made. We use statistically robust methods to assess the relationships – both linear and nonlinear.

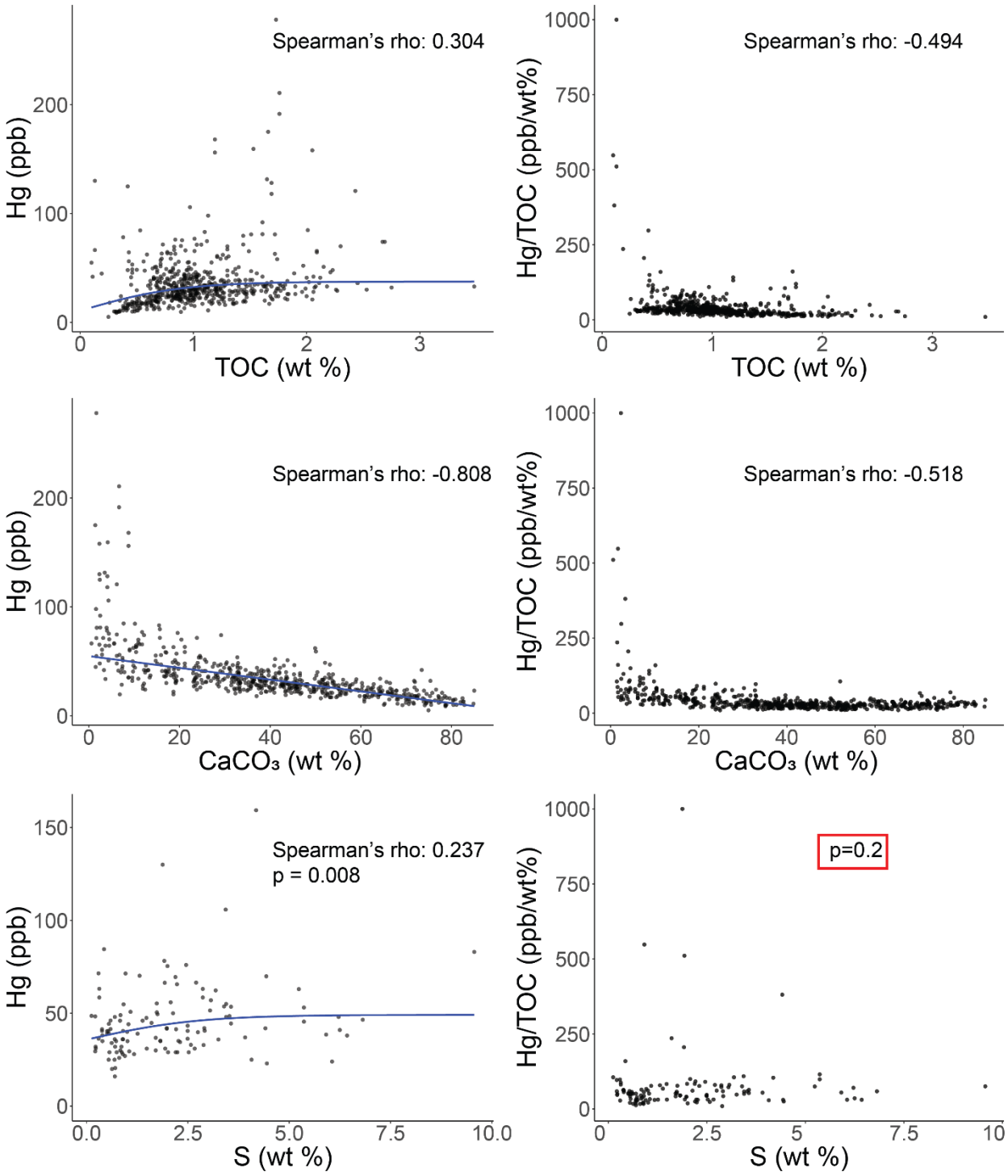

Figure S3: Hg vs. TOC, $CaCO_3$, and S for the Mochras dataset – In the left set of figures, we show the relationship between sedimentary Hg and TOC, $CaCO_3$, and S (along with the fits for the relationship between Hg and these phases) while on the right we show these relationships vs Hg/TOC. Each plot shows the correlation using Spearman's rho (ρ) (two-sided test). We use Spearman's rho because it does not assume linear covariation and instead tests monotonicity: a value of 1 indicates a purely monotonic increasing relationship, and -1 a monotonic decreasing

relationship. Note that this is a correlation test, not an assessment of the best-fit lines shown. Smaller absolute values (< 1) indicate progressively weaker correlations. We demonstrate that $CaCO_3$ has the strongest correlation with Hg (Spearman's rho of -0.8) hence we correct for $CaCO_3$ first. We assess the significance of the correlation with a p value: if no p value is shown, then p<<0.001 and the relationship is statistically significant. When p>0.01, the p value is shown with a red box around it, indicating that no statistically significant relationship is present.

(i) Dilution by calcium carbonate:

Increasing $CaCO_3$ concentration can dilute the concentration of organic or siliciclastic materials, especially in the case of secondary calcite precipitation (e.g., calcite veins). Typically, carbonates exclude Hg during formation (relative to TOC in sediment). Thus, we expect, to first order, that sedimentary carbonate will negatively co-vary with Hg. We find this to be true: out of $CaCO_3$, TOC, and S, Hg is most strongly correlated with $CaCO_3$ (Fig. S3). As each of the common Hg host-phases (e.g., TOC, S) are diluted by $CaCO_3$, we need to account for this when analyzing the Hg concentrations. Other studies have noted these trends also. Hg concentration has been noted in some cases to vary inversely with $CaCO_3$ concentration, particularly in carbonate-rich depositional environments[10]. Biogenic carbonates in some cases also have lower Hg concentration (factor of 2–3 less) than surrounding (non-carbonate) sediments, possibly due to exclusion during formation[10,11].

In the Mochras core, $CaCO_3$ content varies considerably, with concentrations between 0.6% and 85%. Carbonate dilution of organic and siliciclastic material has been explicitly noted in Mochras sediments[3]. The carbonate dilution effect on organic carbon in similar lithologies has previously been corrected, in similar Jurassic lithologies, by calculating a calcium carbonate-free TOC concentration[12]. We follow this approach and calculate the concentrations of Hg, TOC, and S in the calcium carbonate-free portion of each sample using:

$$X_{\mathrm{cf}} = \frac{X}{1 - \frac{CaCO_3}{100}}$$

Equation 1

where X indicates the concentration of Hg, TOC, or S respectively, X_{cf} represents the calcium carbonate-free concentration of the respective species, and $CaCO_3$ is the concentration (weight percent) of calcium carbonate in a particular sample. Note that as $CaCO_3$ concentration approaches 100% the X_{cf} value becomes meaningless (as there is no $CaCO_3$-free portion of the sample). An internal validity check for the application of this approach, to our dataset, is by (a) testing whether there is an overall linear relationship between Hg and $CaCO_3$ and (b) testing whether the samples (or data-based extrapolation) with ~ 100% carbonate have close to zero Hg. As shown in Figure S3, the Mochras data satisfy both tests thus justifying the application of this

method. We would note that for a given sample, Hg/TOC is equivalent to Hg_{cf}/TOC_{cf} – thus normalization of calcium carbonate-free values does not affect the relative data comparison. However, these calcium carbonate-free values allow us to calculate a residual Hg value, as described in the following section. In addition, the calcium carbonate-free correction logically clarifies the chemical relationship between the Hg and the host-phase by effectively removing the non-Hg (and non-TOC) phase from the sediment sample. Note that we calculate the concentration of $CaCO_3$ using published total inorganic carbon (TIC) values[13,14], by assuming all TIC is in $CaCO_3$: $CaCO_3 = TIC \times 100/12$ (as there are 12 g of carbon per every 100 g of $CaCO_3$ by atomic mass).

(ii) Nonlinearity & (iii) quantification of the excess of Hg compared to background:

Conceptually, we expect that there is some relationship between the background (non-excess volcanism/other perturbation affected) Hg and the main host-phases (X_1, X_2, .., X_n for up to *n* phases) of the following form:

$$\mathrm{Hg}_{bkg}(\mathrm{X}_1, \mathrm{X}_2, .., \mathrm{X}_n) = a\, f(\mathrm{X}_1, \mathrm{X}_2, .., \mathrm{X}_n, b) + c$$

Equation 2

where *f* is some mathematical function (linear or nonlinear) and *a*, *b*, and *c* are constants. *c* is the value of Hg_{bkg} at zero concentration of the main host-phases and represents either Hg within a minor phase (or free Hg phase). The measured Hg in a given sample will be thus a combination of expected background Hg and the excess Hg (Hg_{excess}):

$$\mathrm{Hg}_{measured} = \mathrm{Hg}_{bkg}(\mathrm{X}_1, \mathrm{X}_2, .., \mathrm{X}_n) + \mathrm{Hg}_{excess}$$

Equation 3

One simple choice for the function *f* is a linear function and *only a single phase* (e.g., TOC) dependence leading to:

$$\mathrm{Hg}_{bkg} = a\,TOC + c \rightarrow \frac{\mathrm{Hg}_{bkg}}{TOC} = a + \frac{c}{TOC} \quad \& \quad \frac{\mathrm{Hg}_{measured}}{TOC} = a + \frac{c}{TOC} + \frac{\mathrm{Hg}_{excess}}{TOC}$$

Equation 4

If *c* is approximately equal to zero (such that $\frac{c}{TOC}$ is always much smaller than $\frac{\mathrm{Hg}_{excess}}{TOC}$), and assuming the slope of Hg *vs* TOC has a constant value of *a*, then $\frac{\mathrm{Hg}_{measured}}{TOC} \propto \frac{\mathrm{Hg}_{excess}}{TOC}$. The use of $\mathrm{Hg}_{measured}$/TOC as a proxy for excess Hg thus relies on these assumptions (constant slope *a*, negligible offset *c*) to analyze changes in Hg_{excess} and TOC within the dataset. Note that direct comparison of Hg/TOC across datasets is only valid under the additional strong assumption that *a* has a single, global value across different environmental settings.

However, the linear assumption underlying the usage of Hg/TOC values is not supported in many sites across a variety of depositional settings: nonlinearity in Hg *vs* TOC occurs in terrestrial and marine environments, in the modern environment and within the geological past. For example, nonlinear Hg-OC (TOC or dissolved organic carbon) relationships have been explicitly described in terrestrial soil, lacustrine, and permafrost environments[15–17]. Furthermore, several marine sediment datasets from modern environments and the geological past also exhibit nonlinearity[10,18] (Fig. S4). However, this nonlinear relationship is usually not noted in studies working with deep-time sedimentary successions, nor is the robustness/validity of linear relationships (besides testing for a linear correlation) investigated in many studies. Many datasets, including the Mochras dataset (Fig. S3), follow a similar trend in which Hg may increase quasi-linearly with low values of TOC, but then plateauing at higher TOC concentrations (Fig. S4., e.g., datasets from Jin et al., 2012[19]; Percival et al., 2018[10]; and Shen et al., 2019[18]; 2020[4]). Nonlinearity in Hg *vs* TOC may suggest that another variable exerts some controlling influence on Hg, or that Hg deposition is controlled by environmental Hg availability at higher TOC concentrations rather than TOC binding site availability. Schuster et al. (2018)[16] term this regime as **flux-limited** rather than the **receptor-limited** quasi-linear regime at low TOC concentrations.

We note that our discussion here does not suggest that calculating Hg/TOC is always an incorrect approach for analyzing sedimentary Hg concentrations. Instead, we posit that a linear regression model (to estimate *a* and *c* values) should be used to test whether the background Hg values in the dataset can indeed be well represented by the linear model underlying the validity of Hg/TOC values. One graphical method to test the presence of nonlinear behavior is plotting Hg/TOC vs TOC. As shown in Figure S3 with the Mochras data, Hg/TOC still co-varies with TOC (Spearman's rho of -0.5, demonstrating a significant negative correlation). This suggests that either the coefficient *c* is not zero and/or Hg_{excess}/TOC still retains some correlation with TOC (and hence the phase dependence has not been taken out completely by normalizing to TOC). In each scenario, we are not satisfying the assumptions for the validity of the Hg/TOC metric. This dependence of Hg/TOC on TOC has been noted previously especially for samples with very low TOC since these will have very high Hg/TOC values unless the coefficient *c* is zero. Furthermore, these samples can also be problematic because of higher analytical uncertainty on TOC concentrations[7]. This problem has been previously addressed by eliminating data that have TOC < 0.2%, because these TOC values are analytically more uncertain[4,7]; however, this approach has the disadvantage of reducing the amount of data available for interpretation. Additionally, it does not correct data at higher TOC concentrations which may have the inverse problem of artificially suppressed values of Hg/TOC due to being in the plateau part (flux-limited regime) of the Hg *vs* TOC curve if the underlying relationship is nonlinear.

Instead of normalization, in our analysis we find a best-fit curve to account for a potentially nonlinear functional relationship between Hg and TOC (and any other host-phase). We subsequently calculate the residual to this curve: the difference between the measured Hg value for a sample and the expected background Hg for that sample based on its TOC or other host-phase content (i.e., the value of the best-fit curve at the corresponding host-phase coordinate). Calculating this value, which we refer to as "residual Hg" (Hg_R), is more useful for our purposes than Hg/TOC because it is physically and conceptually more directly relatable to the excess Hg emissions from LIP volcanism. Assuming we fit the best-fit curve well, then residual Hg is closely related to Hg_{excess}.

Additionally, we can easily extend the curve fitting methodology to account for co-variation with multiple parameters at the same time. These can be separable functions – $\mathrm{Hg}_{bkg} = a_1\, f_1(\mathrm{X}_1, b_1) + a_2\, f_2(\mathrm{X}_2, b_2) + \cdots + a_n\, f_n(\mathrm{X}_n, b_n) + c$ – and can hence can be evaluated in sequence one host-phase at a time or together for joint relationships – $\mathrm{Hg}_{bkg}(\mathrm{X}_i, \mathrm{X}_2, .., \mathrm{X}_n) = a\, f(\mathrm{X}_1, \mathrm{X}_2, .., \mathrm{X}_n, b) + c$. Furthermore, we can explicitly account for the type of relationship (linear or nonlinear) present in a particular dataset by choosing different types of mathematical forms for the function(s) *f*. Even for linear Hg *vs* TOC relationships, a residual rather than a normalization (scaled) approach presents an advantage because it does not lead to very high values at lower TOC concentrations – as we are not dividing by increasingly small numbers. As a result, our proposed approach is less affected by the analytical uncertainty at low TOC concentrations. Finally, we can more easily compare datasets across different localities since we directly estimate Hg_{excess} – *a physically relatable quantity*.

One potential challenge with our approach is that it requires a sufficiently large dataset such that background conditions (i.e., periods with no reason for us to suspect a perturbed Hg cycle) make up a significant amount of the data used to determine the best-fit curve. We however note that the Hg/TOC approach is also not immune to this challenge since some background value of Hg/TOC value (and hence a value for the Hg_{bkg}) still needs to be chosen in order to identify peaks.

There are many ways to determine a best-fit curve. Here, we use robust nonlinear regression because of the high likelihood of outliers due to non-host-phase-driven Hg increase caused, for example, by volcanically derived Hg in the dataset (non-zero Hg_{excess}). Robust regression uses iteratively reweighted least squares regression to specifically account for the presence of outliers in the data. We use R package robustbase version 0.93-9 function nlrob()[20] (see S6 for an example of code to generate Hg_R). The result of this iterative regression is that each datapoint is assigned a weight between 0, a completely rejected outlier, and 1, a completely included inlier.

Using robust nonlinear regression (or any other regression method) requires us to provide the mathematical form for the regression. Then the best-fit coefficients are found for a particular dataset. For our dataset, we empirically choose the following mathematical functional form, motivated by the two conceptual end-members for sedimentary Hg-host-phase relationship: **flux-limited** and **receptor-limited**:

$$\mathrm{Hg}_{bkg} = a \times \tanh\left({}^{X}/_{b}\right) + c$$

Equation 5

where X is the concentration of TOC or any other host-phase, identified by the presence of positive-sloped co-variation with Hg concentration. Hyperbolic tangent functions, with different values of the coefficients a & b can effectively represent both a positively sloped linear type relationship as well as smooth transition to a constant plateau at larger values of X. This follows from the previously noted trend of an initial approximately linear increase in Hg at low X values followed by a plateau at high X values. The tanh form also has the advantage of coefficients that are intuitive from examining the data by eye: b is the "hinge point" – the value of X at which the slope starts strongly decreasing towards a Hg plateau, a is the value of Hg at which the curve plateaus, and c is the value of Hg when X is 0. In cases where Hg *vs* X is quasi-linear (the assumption underlying the Hg/TOC metric), coefficients a and b are not individually meaningful but generally b is greater than the highest included X value. In these cases, the best-fit coefficients specify a curve that is quasi-linear within the region of the fitted data. Thus, our proposed method does not bias us against a simple linear relationship between Hg and the host-phase X. However, it is a more flexible, and in our opinion, more mathematically transparent analysis approach to infer Hg_{excess}. Estimating the Hg_{excess} value, and thus quantitative volcanic gas emissions (as done in the main text) is not possible from the $\mathrm{Hg}_{\mathrm{measured}}$/TOC metric directly without further assumptions.

We emphasize that the choice of function form we use in this study is dependent on first examining the data (our dataset as well as a number of other sedimentary Hg datasets) along with some conceptual understanding of Hg-host-phase relationships. The two end-members - flux-limited (supply limited) and receptor-limited (akin to kinetically limited) – are frequently used for modeling large-scale chemical reaction dynamics (e.g., parameterizations for surface weathering fluxes[21]). In principle, we can generalize the functional choice (including (non-)linear piecewise functions with hinge points – used e.g., by Schuster et al. (2018)[16] to describe Hg in permafrost) by using model selection approaches (e.g., adaptive regression splines) that try to find a balance between model accuracy (estimated by the robust residual standard error) and model complexity (number of free parameters). The best model should be complex enough to

capture key details of the data yet not be too complex to overfit the data. Incorporating robust functional selection methods in our analysis framework is beyond the scope of the present work but can be incorporated in future studies if the tanh function does not explain the measured Hg-TOC (or other phase) relationship. For our dataset, we find that a tanh (hyperbolic tangent) function provides reasonable results and is also physically & empirically well-motivated. In addition, robust regression with a pre-chosen functional form is computationally much faster and more stable than a large functional search.

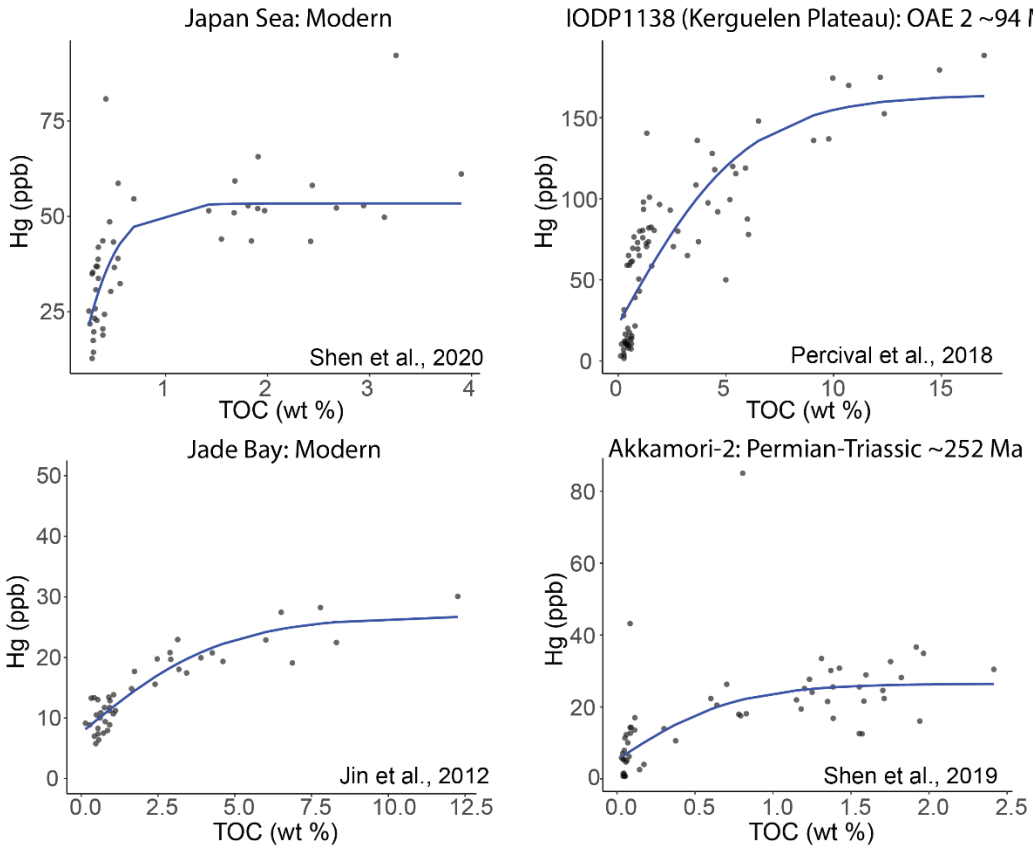

Figure S4: Examples of literature Hg and TOC datasets from marine sediments which exhibit nonlinearity, from both modern datasets (left column)[4,19] and within the geologic record (right column)[10,18]. Each of these best-fit curves was found using the same method described in (ii): nonlinear robust regression with a tanh function. So far, most literature Hg vs TOC patterns examined vary between linear and tanh relationships (if they co-vary at all).

For some datasets, a logarithmic fit can also be attempted. It is often very similar to the tanh fit, although not always: a log fit is generally preferred if the "plateau" still has a small increasing slope. Both functions should be tested in those cases and the one with smaller RRSE should be preferred. The log function we used is: $\mathrm{Hg}_{bkg} = a \times \log_{10}(X/b) + c$, where a, b, and c, are constants and X is the host-phase variable (e.g., TOC, S).

(iv) Multiple potential host-phases:

In many cases, Hg covaries not only with TOC but also with additional parameters, such as sulfur and clay mineral concentration, relations that are often difficult to disentangle since there are relationships between these additional parameters themselves and with TOC. For instance, clay mineral and sulfur content tend to co-vary with TOC[4,10], implying it is difficult to isolate the effects of each of these parameters. In previous work, the covariation between Hg and a non-TOC host-phase has typically been addressed by normalizing Hg to other parameters (e.g., sulfur, aluminum) in the same way as TOC, i.e., by using Hg/S or Hg/Al. The challenge with this approach is that it can only account for co-variation with one control parameter at a time and makes strong assumptions about the functional relationship (see discussion earlier regarding Hg/TOC). Furthermore, if Hg content is not only hosted but also controlled by a number of phases within a single sample of sediment[5,9], accounting for only one of these parameters may incompletely remove biases. In these cases, we need to jointly analyze the controls on Hg_{bkg}: $\mathrm{Hg}_{bkg}(\mathrm{X}_1, \mathrm{X}_2, .., \mathrm{X}_n) = a\, f(\mathrm{X}_1, \mathrm{X}_2, .., \mathrm{X}_n, b) + c$ The best-fit results can be used to explicitly calculate a residual Hg value with its dependence on multiple variables removed (or at least corrected for) at the same time.

If we could assume that host-phases were independent of each other, finding the best-fit function for Hg_{bkg} can be done with multivariate regression, e.g., where we solve for coefficients for an equation that contains both TOC and S at the same time. However, this analysis would yield a unique set of coefficients (robust to noisy data) only if the host-phases were completely independent of each other. This assumption is unlikely to be valid because a large proportion of sulfur is bound in organic matter and clay minerals are important organic carbon hosts in marine sediments[6,22]. We therefore recommend performing the Hg-*X* (host-phase) best-fit regressions in series – first with whichever parameter has the strongest co-variation with Hg, then testing for a relationship between this first residual and the other remaining parameters. If co-variation remains, then a second regression and residual should be calculated. This process can be repeated until there is no remaining statistically significant relationship between the residual Hg and any potential host-phase. For joint, multivariate functional dependence between Hg and host-phases (e.g., $\mathrm{Hg}_{bkg}(\mathrm{X}_1, \mathrm{X}_2) = a\mathrm{X}_1\mathrm{X}_2 + a_2\mathrm{X}_1\mathrm{X}_2^3 + c$), we need to perform joint statistical inversion for a,a_2,c along with two equations for potential relationships between phases X_1 and X_2 ($\mathrm{X}_1 = f(\mathrm{X}_2) + c_1, \mathrm{X}_2 = f(\mathrm{X}_1) + c_2$). In our Mochras dataset, we find that the sequential analysis – first calculating $CaCO_3$-free values and then calculating residual to TOC regression – accounts for the dependence of Hg on host-phases accurately. Thus, we do not use fully generalized, but computationally more expensive, multivariate analysis framework in this study.

S1.3: Results of data analysis for the Mochras dataset:

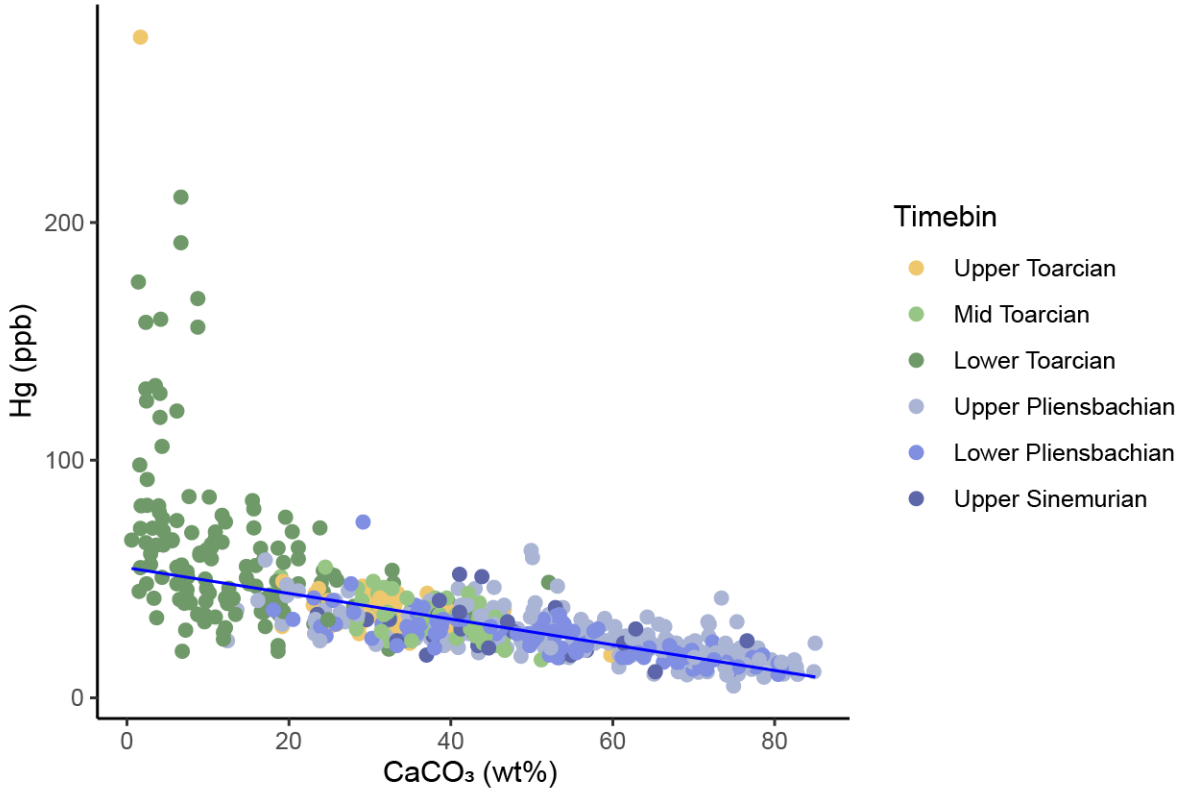

Figure S5: Hg vs $CaCO_3$ for the Mochras dataset with points colored by stratigraphic interval. The best-fit (mixing) curve is consistent throughout the entire record.

We first address the dilution by calcium carbonate, as Hg, TOC, and S are all concentrated in the non-carbonate phase. Accordingly, Hg is most strongly correlated with TOC among these parameters and when we plot Hg *vs* $CaCO_3$ for the Mochras data, we find a negatively sloped linear relationship between the two (Fig. S3). The best-fit relationship can be calculated using robust linear regression (expected formula $\mathrm{Hg} = A \times \mathrm{CaCO_3} + B$) is:

$$\mathrm{Hg} = -0.5 \times \mathrm{CaCO_3} + 50$$

Equation 6

where Hg is in ppb (ng/g) and $CaCO_3$ is in weight percent (robust residual standard error, RRSE, of 7.85 ppb).

This equation is consistent with mixing between a $CaCO_3$-free end-member with a concentration of ~50 ppb Hg and a 100% $CaCO_3$ end-member with negligible Hg. We also find that this relationship is fairly consistent through depth/time, with the Toarcian OAE interval and associated low $CaCO_3$ concentrations deviating the most from the best-fit line (Fig. S5). As $CaCO_3$ dilution is driving the co-variation between Hg and $CaCO_3$ (satisfies the criteria we

established in section 1.2 (i)), we calculate $CaCO_3$-free values for Hg and TOC (Hg_{cf} and TOC_{cf}) (Fig. S7).

We then calculate residual Hg for the Mochras data with respect to a curve fitted between Hg_{cf} and TOC_{cf} using robust nonlinear regression with a hyperbolic tangent (tanh) function, as described previously (curve shown in Fig. S6, top left plot). Here, the robust residual standard error (RRSE) on the fit is 14.3 ppb (Hg). This means residuals greater than |28.6 ppb| (2×RRSE) are treated as statistically significant outliers. The 95% variability range (-28.6 to +28.6 ppb) is plotted in the main text Fig. 2 as a blue shaded region of the Hg_R plot. Using the Hg_R proxy relies on the assumption that a large fraction of the Hg data is at "background" concentrations, i.e., not elevated due to external processes such as volcanism. We believe this assumption to be valid in our dataset because less variability is exhibited in both raw Hg and Hg/TOC in the lower section of the record (>1000 m depth), and accordingly the residual Hg for most of these data is within the 2×RRSE window.

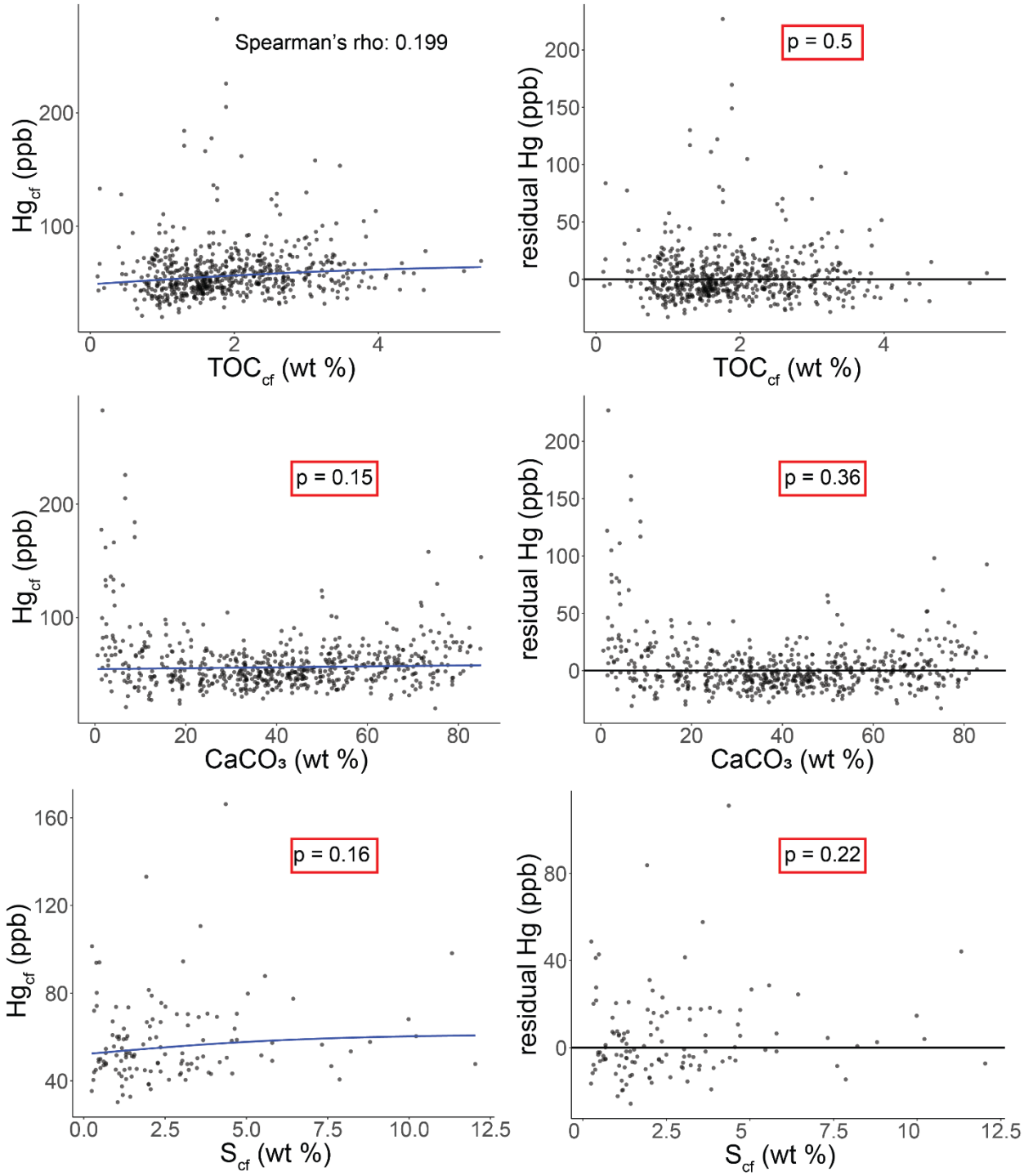

344

345 *Figure S6: Left column: Hg calcium carbonate-free (cf) vs TOC_{cf}, $CaCO_3$, and S_{cf}. The*
346 *blue curves are each calculated using robust regression. Hg_{cf} quasi-linearly co-varies with*
347 *TOC_{cf} and S_{cf}, with a shallow slope in both cases, although the only correlation between Hg_{cf}*
348 *with TOC_{cf} is statistically significant (p values <0.01, in which case Spearman's rho is*

recorded). No correlation remains between Hg_{cf} and $CaCO_3$, demonstrating that the correlation between Hg and $CaCO_3$ was successfully removed. Right column: Residual Hg (calculated with carbonate-free Hg and TOC), vs TOC_{cf}, $CaCO_3$, and S_{cf}. These plots show that no statistically significant correlation remains between residual Hg and any of these species, including S_{cf}, which is not explicitly accounted for. Note that the sulfur plots (a & b) only show the subset of the Hg sample set which have S data.

We use residual Hg, (Hg_R) the calculated residuals with respect to this curve, as a Hg chemostratigraphic index that is explicitly calculated to be independent of the influence of TOC and $CaCO_3$. We test whether residual Hg is independent of these parameters as well as sulfur in Fig. S6, where we plot residual Hg versus carbonate-free TOC and sulfur, and $CaCO_3$ concentrations. We find that no statistically significant correlation remains between residual Hg and any of these parameters, and that elevated values of residual Hg are not confined to the low TOC and $CaCO_3$ samples. Interestingly, while we do not explicitly account for co-variation between Hg and sulfur, residual Hg does not seem to significantly correlate with sulfur, likely due to co-variation between TOC and/or $CaCO_3$ and sulfur (Fig. S6). **In the Mochras dataset, while Hg *vs* TOC is nonlinear (Fig S2), Hg_{cf} vs. TOC_{cf} is quasi-linear (with a shallow but non-zero slope) (Fig S5), suggesting that the nonlinearity in the first case is at least partially due to correlation between Hg, TOC, and $CaCO_3$.**

When we plot residual Hg stratigraphically and compare with Hg, Hg_{cf}, and Hg/TOC (Fig. S7), we see that similar patterns are observed in all three parameters for the Sinemurian, lower Pliensbachian, and mid to upper Toarcian, all of which are mostly within background range of variability. All three datasets also exhibit significant peaks in the lower Toarcian. The datasets differ most in the upper Pliensbachian (~900 – 1000 m core depth), which exhibits peaks in residual Hg but less variability in Hg/TOC and raw (measured) Hg. This pattern is explained by looking at calcium carbonate-free Hg, which also has peaks in this interval. It follows that the Hg in this interval are artificially suppressed by high calcite concentrations, which is consistent with the observations of abundant secondary calcite veins in the upper Pliensbachian[23]. That the calcite is secondary further supports the decision to use calcium carbonate-free Hg and TOC to calculate the residual.

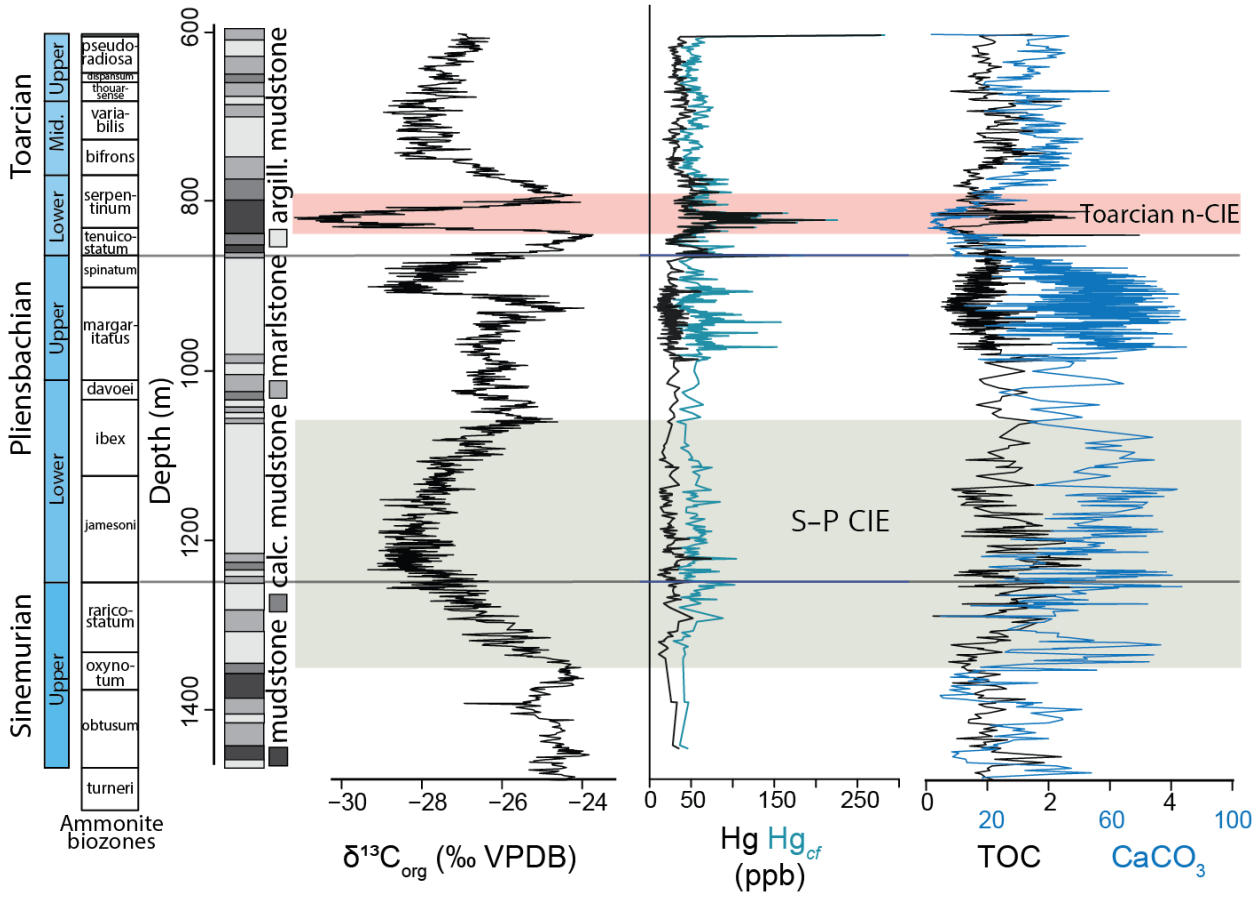

Figure S7: Mochras ammonite biostratigraphy[24,25] and lithological log[23] plotted alongside chemostratigraphy versus core depth (mcd): left plot shows organic-carbon isotopic composition[13,14] ($\delta^{13}C_{org}$); middle plots shows Hg and $CaCO_3$-free Hg (Hg_{cf}) concentrations (this study); right plot shows total organic carbon (TOC) and $CaCO_3$ concentrations[13,14]. The Sinemurian–Pliensbachian (S-P) and T-OAE n-CIEs are indicated.

S2: Processes other than volcanism which may affect Hg records:

Redox & diagenesis

Sedimentary mercury and TOC or S-normalized Hg records can be impacted by various redox fluctuations and diagenetic processes[4,26]. For example, aerobic degradation of organic matter and sulfides has a tendency to reduce the quantity of the host-phases retained in the sediment while, in these conditions, Hg appears less mobile[26], similar to oxidative weathering of exposed surfaces[27]. In contrast, it was recognized that deoxygenation, in cases where (bottom) waters are anoxic but not strongly euxinic may lead to reduced (normalized) Hg burial, which is particularly pronounced when normalizing to both TOC and S[26]. Whether this has also reduced Hg or Hg_R in some intervals of the Mochras core is not certain but partial Hg loss may imply Hg and Hg_R are

conservative estimates of the primary Hg flux. We note that while such effects may come into play (Fig. S4), the impact of reduced Hg burial relative to common host-phases may be largely eliminated by accommodating non-linear behavior between Hg and host-phases.

In contrast to these mechanisms that may induce a reduction in Hg or normalized Hg, Hg enrichments have also been documented. Diagenetic pyrite[4,28,29], occurs within the Mochras sequence and may have focused Hg in (parts of) the stratigraphy. However, as we see no clear relation of Hg with TS beyond the sulfur included in organic matter (see discussion above) we surmise that diagenetic Hg enrichment in pyrite is not a major factor in the Mochras material. Lastly, Hg focusing may occur around buried redox fronts[26,30], which are difficult to pinpoint in geological records. While we have no direct control on the presence or absence of extinct redox fronts, such effects are expected to be uncommon in sequences with near-continuous, quasi-stable, sediment accumulation such as recovered in the Mochras core.

Weathering:

Terrestrial sediments and organic material are a major source of Hg to modern and Jurassic near-shore marine environments[31,32]. This spatial pattern is primarily of concern when comparing Hg records between locations or, in our case, between data and Hg box-model results. We first evaluate Hg enrichment relative to site-specific background (enrichment factors shown in Fig. 3 in main text), and subsequently extrapolate Hg enrichment to global Hg loading.

Major changes in weathering likely affect the Hg cycle – increasing fluxes of material from the continents to the ocean would undoubtedly increase the flux of Hg to the ocean as well. Most weathered Hg is originally contained within terrestrial surficial sediments and biological materials – so likely to have been taken up from atmosphere within the previous ~1000 years (based on residence timescales from modern environments)[32,33]. This is within the temporal resolution of our dataset and so influxes of weathered material are unlikely to significantly change the pattern recorded in marine sediments in an unrepresentative manner (as increased Hg availability in the environment due to increased Hg loading from volcanism will affect each of the reservoirs). The box model we use to scale Hg enrichment in Mochras sediments to Hg emissions also includes the quantity and temporal effects of cycling within the terrestrial environment prior to transport to the ocean.

However, for an increased weathering flux to lead to an increase in residual Hg assumes Hg is not transported as a particulate already within some host-phase, i.e., correcting for changing host-phase deposition does not sufficiently correct for effect of increased Hg from run-off. This is generally unlikely to be the case as studies on modern riverine Hg demonstrate the vast majority of riverine Hg is transported in the particulate phase (usually attached to particles of organic carbon)[34].

Fire:

Gaseous Hg can be released by major fire events[35]. However, we do not see sample-by-sample co-variation between residual Hg and charcoal (derived from wildfire) within Mochras, when data is available from the same core depth (charcoal data from Hollaar et al., 2021[36]) (Fig. S8). Although transport to sedimentary archives likely differs for Hg and charcoal, this lack of co-variation does not support a significant wildfire flux for the Hg signals recorded in the Mochras core.

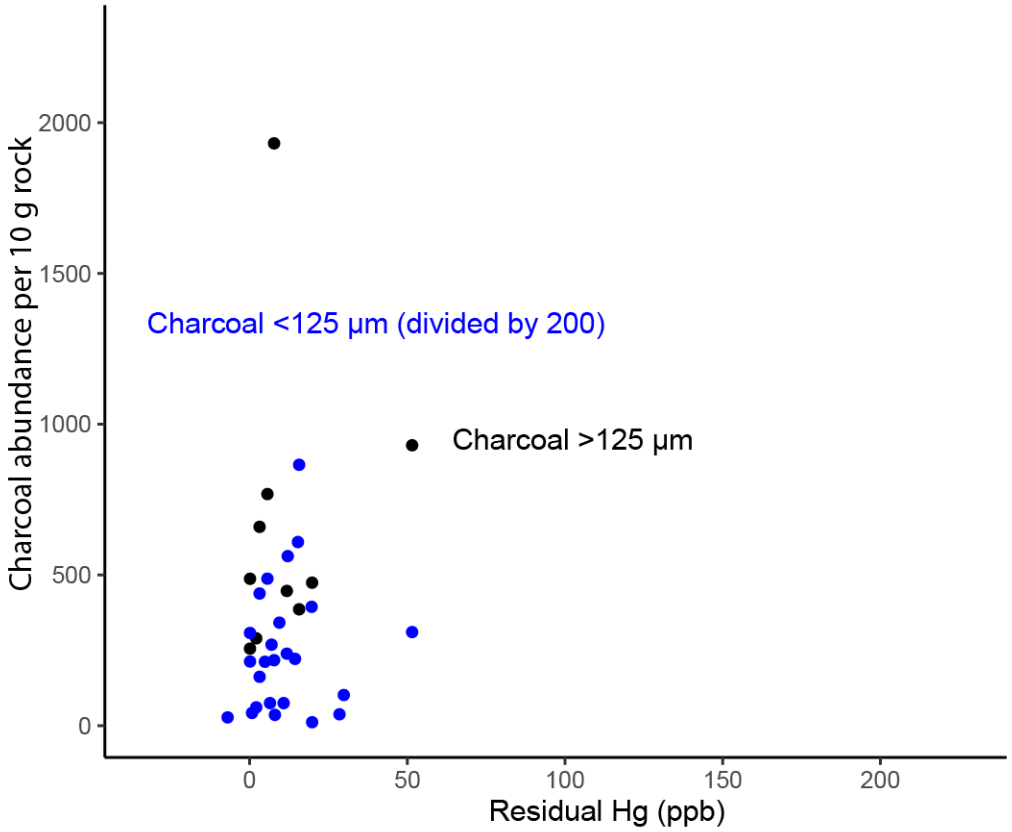

Figure S8: Charcoal abundance[36] vs. residual Hg in the Mochras core samples. To enable plotting both charcoal-particle datasets on a single y-axis, we linearly rescale the <125µm charcoal abundance by a factor of 1/200.

S3: Age model & sample availability:

The Mochras core samples analyzed within this study are archived at the National Geological Repository of the British Geological Survey, Keyworth, UK. The lithology throughout the core is dominated by marls with variable amounts of calcium carbonate content: some sections being carbonate-rich (~80%) and others, especially the Toarcian OAE interval,

being almost entirely carbonate-free[23]. The non-carbonate fraction comprises clay minerals and organic material.

For the Sinemurian and Pliensbachian intervals we use the relative astrochronological age model created by Storm et al. (2020)[13], which we tie to the Pliensbachian–Toarcian boundary at 183.73 Ma[37] (based on a radioisotopic date). For the Toarcian, we use an approximate age estimate by linearly interpolating between ammonite biozone boundaries, using dates from the Geological Time Scale 2020[38], except for the *tenuicostatum–serpentinum* zonal boundary for which we use a date of 182.77 Ma[37]. The depth of ammonite biozonal boundaries within the Mochras record are from Ivimey-Cook (1971)[25], revised in Copestake & Johnson (2013)[24]. While linear interpolation does not constitute a robust age model *per se*, the relatively short time interval within each biozone (generally <1 Ma) make this approach in this case adequate for comparison with dates from the Karoo-Ferrar LIP and other external constraints, given the uncertainties also associated with these other data.

The discrepancy in duration of the T-OAE n-CIE between our age model for the Mochras borehole record and the age models used in the two model scenarios cited is not novel: a similar discrepancy has been previously noted in several other locations. A duration of ~900 kyr has previously been hypothesized if the primarily sedimentary cycles (found via cyclostratigraphy) are correlated with ~100 kyr short eccentricity astronomical cycles[39–41]. However, an alternative is that the cycles instead correspond with the ~35 kyr obliquity astronomical cycles, resulting in the n-CIE having a shorter duration of 400–500 kyr[42].

In our age model, the duration of the n-CIE is determined primarily by the recently published radioisotopic dates (U-Pb dates on zircon) and associated age model of the Pliensbachian–Toarcian boundary (prior to the n-CIE) and the *tenuicostatum–serpentinum* zonal boundary (during the n-CIE), both from the Neuquén basin, Argentina[37]. This duration is compatible with the eccentricity-modulated age model.

S4: Hg & CO_2 emissions estimates:

S4.1: Estimation of Hg emissions:

We calculate Hg enrichment by dividing the residual Hg value by the expected Hg value at that data point (the point on the final best-fit curve at the calcium carbonate-free TOC value for each sample – Fig S6) and adding 1 such that the background data have an enrichment factor of 1 (on the best-fit curve, $Hg_R = 0$). The slope on the Hg_{cf} vs. TOC_{cf} best fit curve is very small for our data (Fig S6, upper left plot) and hence this is almost equivalent to dividing by a constant

(enabling us to have a secondary axis for approximate enrichment factor on the plot of residual Hg in Fig. 3 of the main text).

Then, we use previously published Hg cycle box model results[43], which used the model from Amos et al. (2014; 2015)[32,33], to scale Hg enrichment to total Hg emission mass, assuming each point represents 1000 years (i.e., 1000-year smoothing window applied to model output) (see Fig S9 and S10). This choice is justified by the typical (median) sedimentation accumulation rate within the Mochras core of ~3.7 cm/kyr, a sample size of 2-3 cm, and bioturbation and/or fluid infiltration leading to mixing of Hg within the top few centimeters of sediment at time of deposition[44]. As a result, the Hg (and CO_2) emissions estimates for each data point are per thousand years (per kyr) (main text Fig. 2). This timescale is also compatible with the duration of noticeably elevated Hg following a typical LIP eruption of >100 years, with sufficient flux(>50 km^3/yr). See Fendley et al., 2019[43] for an expanded discussion of LIP eruption rates, durations, and expected Hg increase in various box-model reservoirs.

We note that if we assumed a more rapid sedimentation rate for the early Toarcian n-CIE (as in other, obliquity-modulated age models – see SI Section 3), this would *decrease* the window size, since a smaller amount of time would correspond with a single sample. This in turn would reduce the Hg emissions which correspond to a given enrichment factor (Fig. S10), and hence result in smaller estimated CO_2 emissions.

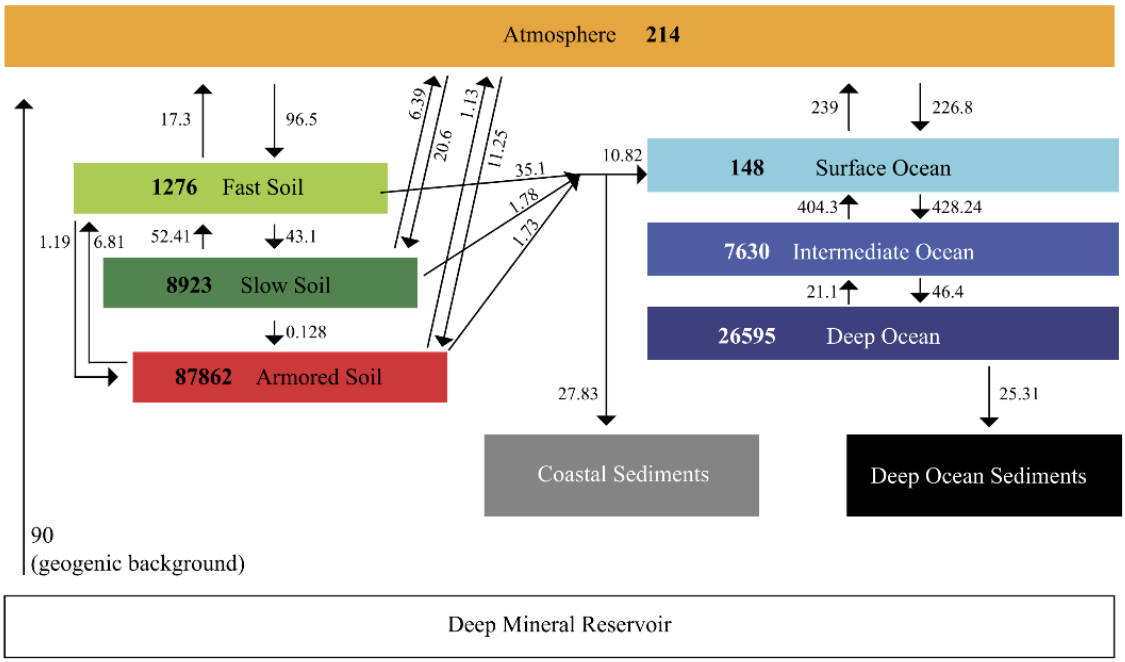

Figure S9: Hg box model used[32,43,45]. The numbers are initial steady-state reservoir sizes and fluxes – these will change in the course of running model scenarios. We compare the Mochras data to the flux into the coastal sediment box. Note that this model assumes the vast majority of coastal marine Hg is sourced from continental runoff, rather than directly from atmospheric deposition – consistent with Hg isotope data across the T-OAE interval from shallow marine settings which suggests a dominantly terrestrial Hg source[31]. However, Hg emissions to the atmosphere propagate through the various reservoirs, resulting in increased Hg emission to both marine sediment boxes (as well as larger amounts of Hg within terrestrial reservoirs).

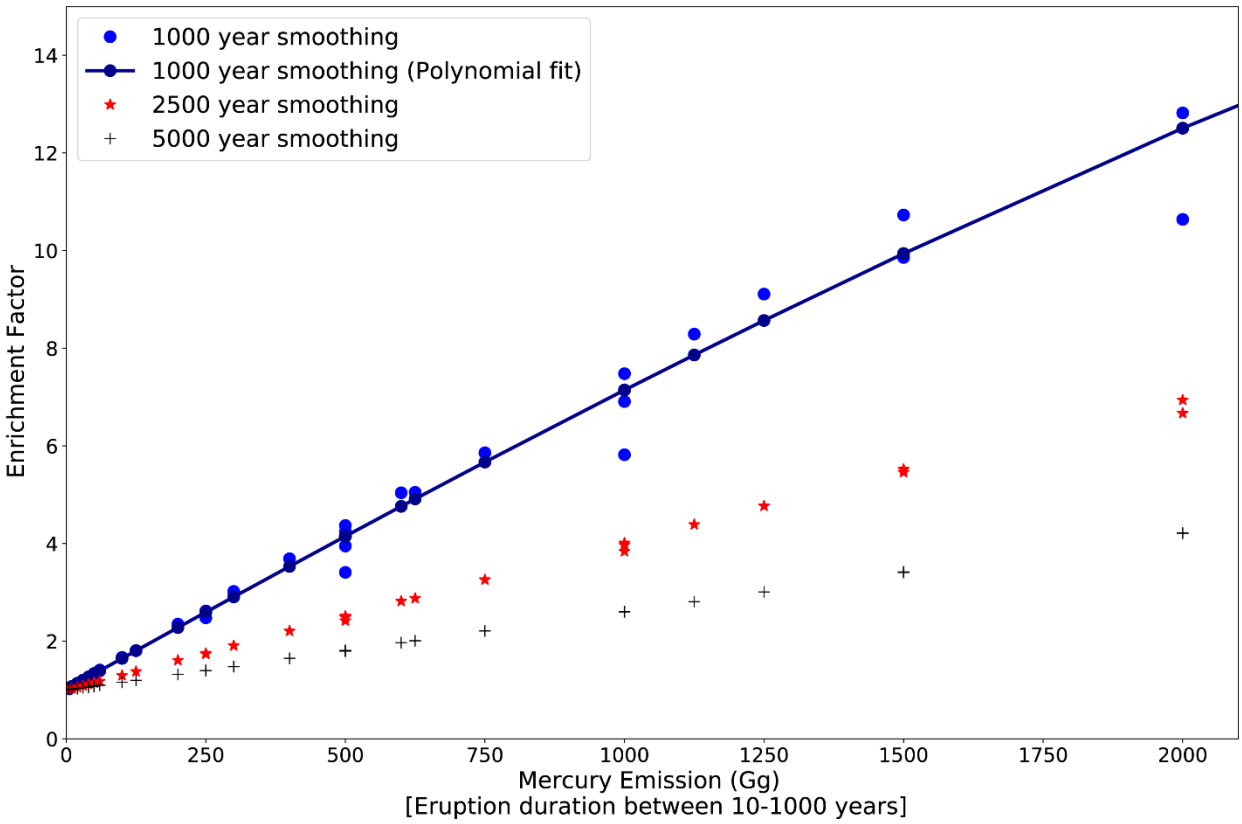

Figure S10: Enrichment factor in the coastal sediment box (which we assume correlates to Hg enrichment factor in Mochras core sediment) as scaled to modelled excess Hg flux to the atmosphere. The 'smoothing' parameter reflects that each point in a sedimentary record reflects a certain amount of time (1000, 2500, or 5000 years). In this study we use the 1000-year smoothing points, with a best-fit curve plotted here to interpolate Hg emissions for a given enrichment factor. There are multiple potential enrichment factors per emission amount as in the model simulation both emission rate and duration are varied (duration of "eruption" is 10–1000 years). This affects the resulting enrichment factor somewhat, but only total emission mass (rate × duration) is plotted here. This effect is more pronounced at very high Hg emissions (>1000 Gg, enrichment factors>5). Figure modified from Fendley et al. (2019)[43].

S4.2 Scaling to carbon (CO_2) emissions:

Once we have calculated Hg emissions, we estimate the amount of CO_2 co-emitted using Hg/CO_2 ratios from modern analogues to LIP degassing processes. In main text Fig. 3, we plot the range of Hg/CO_2 ratios from 1×10^{-6} to 1×10^{-7} which accounts for most volcanic (including diffuse) as well as thermogenic emissions (Table S1).

Table S1: measured Hg/CO_2 ratios for several volcanoes and degassing scenarios and estimated and measured Hg/CO_2 release from sediment/coal combustion sources as an analogue for thermogenic emissions.

Hg/CO_2 (mass) × 10^{-7}	**Volcano/source**	**Measured/calc.**	**Setting**	**Reference**
12 to 22	Kilauea	Measured	Halemaumau main vent	Siegel & Siegel (1987)[46]
8.7 to 17	Etna	Calculated from CO_2/SO_2 and Hg/SO_2	Main plume	Bagnato et al. (2007)[47] & Shinohara et al. (2008)[48]
0.5	Campi Flegrei	Measured	Fumarole	Bagnato et al. (2020)[49]
5	Italy (Larderello-Travale geothermal field)	Measured	Soil degassing	Cabassi (2021)[50]
1	Masaya	Measured	Main vent	Witt et al. (2008)[51]
0.1	Masaya	Measured	Low T fumaroles	Witt et al. (2008)[51]
0.14 to 0.46	Furnas	Measured	Various fumaroles and diffuse	Bagnato et al. (2018)[52]
Sediment combustion (thermogenic analogue):				
~3	S. African coal	Calculated assuming complete combustion		Zerizghi et al. (2022)[53]
9.3 to 14.0	Coal fire (USA)	Measured (ratio of total annual emissions)		O'Keefe et al. (2010)[54]
1.7, 0.5, 0.03	Coal fires (USA)	Measured (each # is average of 1 fire)		Engle et al. (2012)[55]
1-0.01	Coal fires (China)	Measured (1 std dev of all data)	In boreholes into soil	Hong et al., (2017)[56]

In general, lower Hg/CO_2 ($<1 \times 10^{-7}$) correlates with lower (<300 ºC) temperature diffuse degassing (often through soil), for both volcanic and sediment combustion sources. This is possibly because of preferential Hg recapture (compared to CO_2) by sediment prior to reaching

the surface. However, to match the total emission rates in the GEOCLIM[57] and COPSE[58] models, Hg/CO_2 would have to have been < ~2×10^{-8} on average. Such values seem unlikely to represent net LIP emissions as KFLIP had a significant eruptive component (up to 5 million km^3)[59] as well as emissions pathways which gas from the intrusive component may have followed (e.g., including rapid explosive venting via breccia pipes)[60] rather than only slowly percolating through thick soil horizons, or other subsurface sediments and groundwater.

We present a wide range of Hg/CO_2 that incorporates the eruptive, intrusive, and thermogenic gas emissions which are hypothesized to account for the vast majority of LIP gas emissions, so we expect that the average or net Hg/CO_2 for LIP volcanism is within our stated range. Although some sources of LIP CO_2 may be decoupled from Hg emissions (e.g., exsolution of CO_2 from very deep intrusive magma bodies), the significance of these processes to overall LIP volatile budgets and their dynamics (e.g., extent of Hg and CO_2 release and transport to surface) remain highly uncertain[61]. We then calculate the equivalent C emissions (from CO_2), based on 12 g C per 44 g CO_2.

Lastly, we apply a 300 kyr moving window sum (step size 50 kyr) to approximate the effect of C accumulation in the exogenic carbon pool prior to loss via $CaCO_3$ precipitation and/or organic carbon burial. This window size is determined by average silicate weathering timescales[62]. This rolling window sum estimates the total C added to the exogenic carbon pool, which makes these estimates comparable to the records of changing pCO_2 and environmental change (including $\delta^{13}C_{org}$).

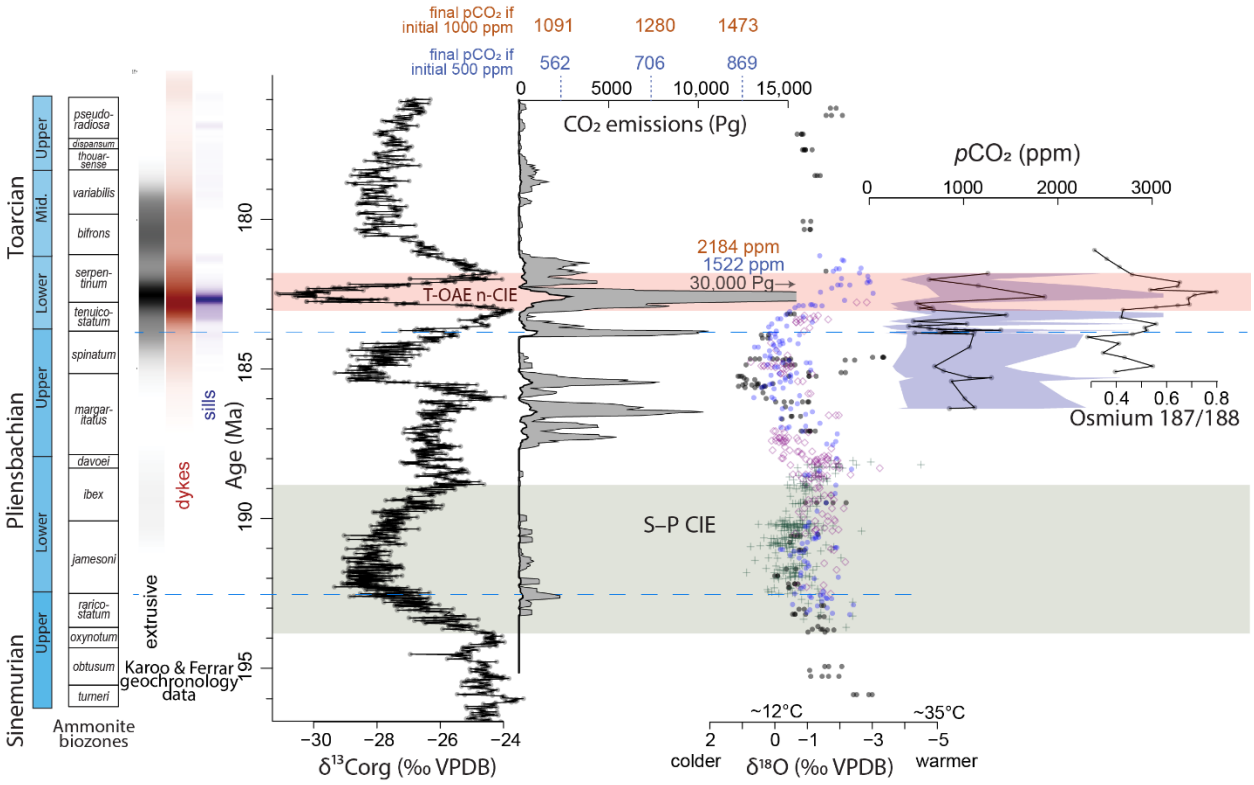

*Figure S11: CO_2 emissions per kyr estimated using enrichment in residual Hg. Note that this figure does **not** use a rolling window sum, unlike main text Fig. 3. Also plotted:belemnite oxygen isotope composition compilation from Tethys and unrestricted Laurasian seaway localities (Mochras/Cardigan Bay basin[23]: grey points, Asturian basin[63]: blue points, Dorset/Wessex basin[64]: green pluses, Cantabrian basin[65]: purple diamonds), pCO_2 changes estimated from B isotopic composition (1 σ uncertainty shown in blue shaded region)[66], and osmium isotope composition from Mochras[2]. The approximate temperature range on the oxygen isotope axis is based equilibrium isotope fractionation between calcite and seawater[67] with $\delta^{18}O_{sw}$ = -1‰. Age models for the oxygen isotope compilation and pCO_2 proxy record are based on either a) using existing age models but tying to the same biozone boundary ages as in the Mochras record or, or if there is no existing age model, b) linearly interpolating between biozone boundaries. In both cases the emphasis is on creating records which are directly comparable to the Mochras data.*

S4.3: Resulting change in pCO_2:

We calculate the approximate final pCO_2 value following these emissions, assuming a constant initial pCO_2 of 500–1000 ppm, using ocean/atmosphere equilibrium carbon partitioning equations for the modern ocean[68]. This is a simple three-box model (deep ocean, surface ocean, atmosphere). In the following equations and discussion, we briefly summarize the model of Devries et al. (2022)[68]. An in-depth analysis of the validity of these approximations is beyond the scope of this study.

In order to estimate the resulting change in pCO_2, we must evaluate how much of the added CO_2 pulse is dissolved in the ocean (as opposed to staying in the atmosphere). This is described using the parameter of seawater equilibrium carbon capacity, *F*, which is defined as:

$$F = {\mathrm{DIC}}/{pCO_{2,sw}}$$

Equation 7

where DIC is the concentration of dissolved inorganic carbon within the ocean (µmol/kg) and $pCO_{2,sw}$ is the partial pressure of CO_2 in seawater (µatm). *F* has units of mol air/(kg seawater).

We describe the carbon pools in the atmosphere and ocean respectively as (note pCO_2 in air is distinct from $pCO_{2,sw}$ in seawater previously discussed – although at equilibrium they are equivalent):

$$C_{atm} = M_{atm} \times pCO_{2,air}$$

Equation 8

and

$$C_{oce} = M_{oce} \times \mathrm{DIC}$$

Equation 9

Where M_{atm} is the mass of the atmosphere (mol), C_{atm} is the mass of carbon in the astmosphere (GtC), M_{oce} is the mass of the ocean (kg), and C_{oce} is the mass of carbon in the ocean (GtC).

At equilibrium, $pCO_{2,air} = pCO_{2,sw}$. So, we can combine the preceding three equations such that:

$$\frac{C_{oce}}{C_{atm}} = F\frac{M_{oce}}{M_{atm}}$$

Equation 10

Now, if we subdivide the ocean into surface and deep components such that:

$$C_{oce} = M_{oce,s}\mathrm{DIC}_s + M_{oce,d}\mathrm{DIC}_s$$

Equation 11

where the subscripts s and d refer to the surface and deep ocean respectively, the partitioning of carbon between the atmosphere and ocean (Equation 10) is adjusted such that:

$$\frac{C_{oce}}{C_{atm}} = F\left(\frac{M_s}{M_{atm}} + \frac{\mathrm{DIC}_d}{\mathrm{DIC}_s} \times \frac{M_d}{M_{atm}}\right)$$

Equation 12

As the amount of carbon within the surface ocean is insignificant compared to the amount within the deep ocean, we can approximate M_s as 0 and M_d as M_{oce}, so:

$$\frac{C_{oce}}{C_{atm}} = F \times \frac{M_{oce}}{M_{atm}} \times \frac{\mathrm{DIC}_d}{\mathrm{DIC}_s}$$

Equation 13

Now, we define the total exogenic carbon pool (C_{tot}), to which we will add our additional CO_2 emissions, as:

$$C_{tot} = C_{atm} + C_{oce}$$

Equation 14

so:

$$\frac{C_{oce}}{C_{atm}} + 1 = \frac{C_{tot}}{C_{atm}}$$

Equation 15

We now combine this with Equations 8 and 13:

$$\frac{C_{tot}}{M_{atm} \times p\mathrm{CO}_2} = F \times \frac{M_{oce}}{M_{atm}} \times \frac{\mathrm{DIC}_d}{\mathrm{DIC}_s} + 1$$

Equation 16

In the pre-industrial ocean, $\mathrm{DIC}_d/\mathrm{DIC}_s$ = ~ 1.1, $M_{atm} = 1.77 \times 10^{20}$ mol air, and $\frac{M_{oce}}{M_{atm}}$ = 7.8 kg seawater (mol air)$^{-1}$.

Devries et al. (2022)[68] used a large compilation of seawater DIC and alkalinity (from Global Ocean Carbon Data Analysis Project version 2, GLODAPv2.2021[69]) to calculate seawater $p\mathrm{CO}_2$ using the CO_2 chemistry module CO2SYS. The results of this analysis, over the range of $p\mathrm{CO}_{2,sw}$ commonly found in modern seawater (100-1000 ppm), yield an empirical fit for F such that:

$$F = 0.23 + {}^{2233}\Big/\left(p\mathrm{CO}_{2,sw} + 34\right)$$

Equation 17

where F is in units of mol air (kg seawater)$^{-1}$. Recall at equilibrium $p\mathrm{CO}_{2,air} = p\mathrm{CO}_{2,sw}$. Therefore, at t = 0, we plug in these values to find that the initial total carbon reservoir size is:

$$C_{tot,i} = \left[\left(0.23 + {}^{2233}\Big/\left(p\mathrm{CO}_{2,i} + 34\right)\right) \times 7.8 \times 1.1 + 1\right] \times (1.77 \times 10^{20}) \times p\mathrm{CO}_{2,i}$$

Equation 18

As an example, at an initial $p\mathrm{CO}_2$ of 500 ppm then $p\mathrm{CO}_{2,i} = 500 \times 10^{-6}$ and $C_{tot,i} \times \frac{12g}{mol} = 4.126 \times 10^{19}$ g .

Now we add some new amount of CO_2 (in units of mass) such that $C_{add} = CO_{2,add} \times \frac{12}{44}$.

$$C_{tot} = C_{add} + C_{tot,i}$$

Equation 19

$$C_{add} = \left[\left(0.23 + {}^{2233}/_{(p\mathrm{CO}_2 + 34)}\right) \times \frac{M_{oce}}{M_{atm}} \times \frac{\mathrm{DIC}_d}{\mathrm{DIC}_s} + 1\right] \times M_{atm} \times p\mathrm{CO}_2 - C_{tot,i}$$

Equation 20

We use the same values for DIC_d/DIC_s, M_{atm}, and $\frac{M_{oce}}{M_{atm}}$ as stated previously to evaluate C_{add} as a function of pCO_2.

We plug in a range of pCO_2 values (step size = 1 ppm) between $pCO_{2,i}$ and 2500 ppm for $pCO_{2,i}$ values of 500 and 1000 ppm (Fig. S11). We then use these values to "look up" the final pCO_2 for various CO_2 emissions (Fig. S12, main text Fig. 3).

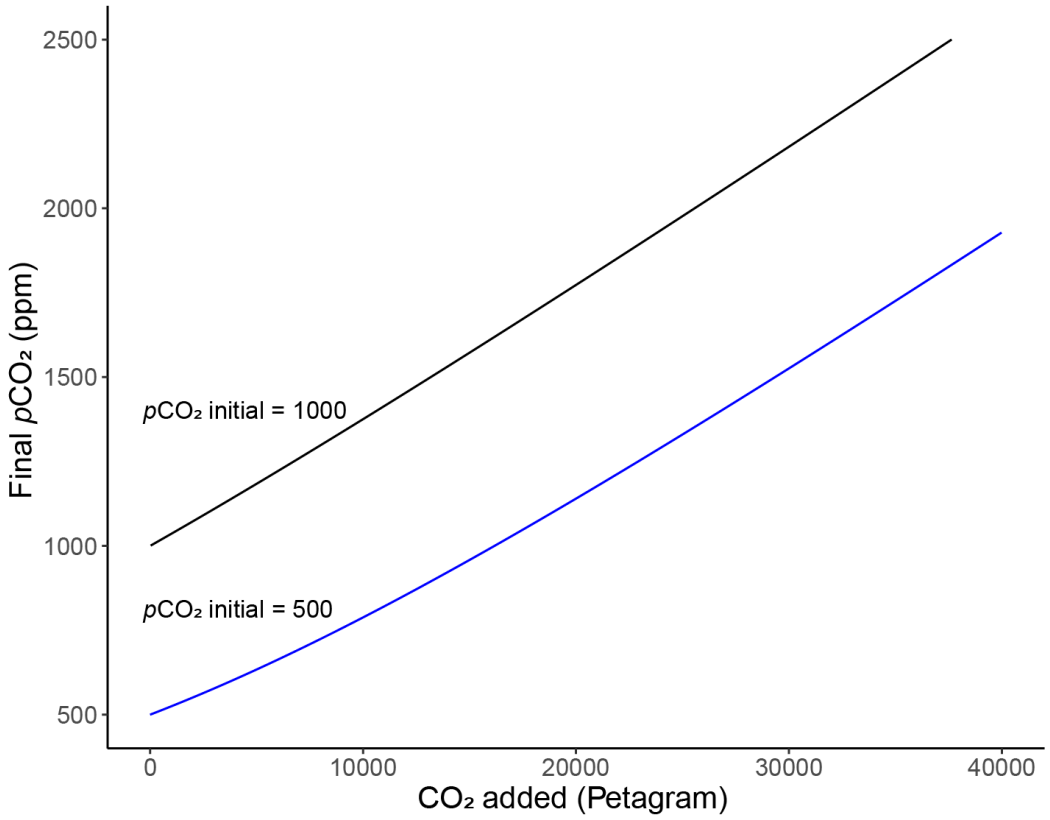

Figure S12: The amount of (instantaneously) added CO_2 needed to result in a range of final pCO_2 values, starting with initial pCO_2 values of 500 ppm (blue line) and 1000 ppm (black line).

S4.4: Comparing with literature model C emissions scenarios:

We compare our estimated C emissions with literature estimates based on matching carbon cycle model outputs with proxy records such as $\delta^{13}C$, pCO_2, and temperature changes. The two studies we reference each used a combination of CO_2 and CH_4 emissions, however, the 'CH_4' and 'CO_2' labels for carbon sources are effectively only used to distinguish between carbon isotope signatures of sources and do not reflect the actual C species represented in these models[57,58]. The choice of carbon compound was important primarily as a ^{13}C depleted component for the carbon isotope composition of the emissions, which is needed in order to match the observed n-CIE. However, the CH_4 in these model scenarios is generally assumed to have no additional impact compared to CO_2 on climate over timescales >1000 years, as it rapidly oxidizes to CO_2 in the atmosphere[58].

We compare our new estimates with the those used in these carbon cycle modeling studies primarily by average C emission rates, in Pg/kyr, in order to best reflect the entire T-OAE n-CIE interval. This comparison is very similar to comparing the average rates during only the falling limb and nadir of the n-CIE. In that case (considering the falling limb only), our Hg-based estimates have a slightly higher average rate than the entire n-CIE duration (0.02 Pg/yr, total of 10,000 Pg C released in 550 kyr), and the Heimdal and Ullmann scenarios remain virtually identical (Heimdal: 80% of the C released during the falling limb, at a cumulative rate of 0.081 Pg/yr, 16,285 Pg C in 200 kyr; Ullmann scenario rate remains 0.54 Pg/yr, 81,000 Pg C in 150 kyr, as all of the C is input during the falling limb).

<u>Heimdal et al. (2021):</u>

This study used the GEOCLIM model to estimate the carbon cycle effects of a series of LIP-associated C pulses, the $\delta^{13}C$ values of which were consistent with a combination of magmatic (CO_2) and thermogenic (CO_2 and CH_4) outputs. We incorporate these C fluxes into our comparison (main text Fig 4 and SI Fig S13), as both magmatic degassing and sediment combustion result in Hg release. The average release rate over the entire emissions period is 0.078 Pg/yr (20,500 Pg C released over 262 kyr).

<u>Ullmann et al. (2020):</u>

This study used the COPSE model to estimate the carbon cycle effects of a combination of LIP-associated CO_2 (dominantly thermogenic) and clathrate-associated CH_4 emissions. We use the scenario presented in their main text Fig 4 (Ullmann SI Fig S12), neglecting the clathrate CH_4 as Hg emissions are hypothesized to only correspond with magmatic and sediment combustion processes. Their emissions scenario is 4.5×10^{13} mol C/yr (0.54 Pg C/yr) for 150 kyr, which is assumed to be a mixture of magmatic and thermogenic CO_2. Their primary goal was to match the temperature increase observed in proxy records; hence, the flux of carbon is a key output. The

larger C emissions estimates in the Ullmann et al. (2020) scenario compared to the Heimdal et al. (2021) scenario are likely partially driven by the former's choice of a larger initial exogenic carbon reservoir (and hence pCO_2, Ullmann: 2–4 × PAL, or 560–1120 ppm; Heimdal: ~500 ppm).

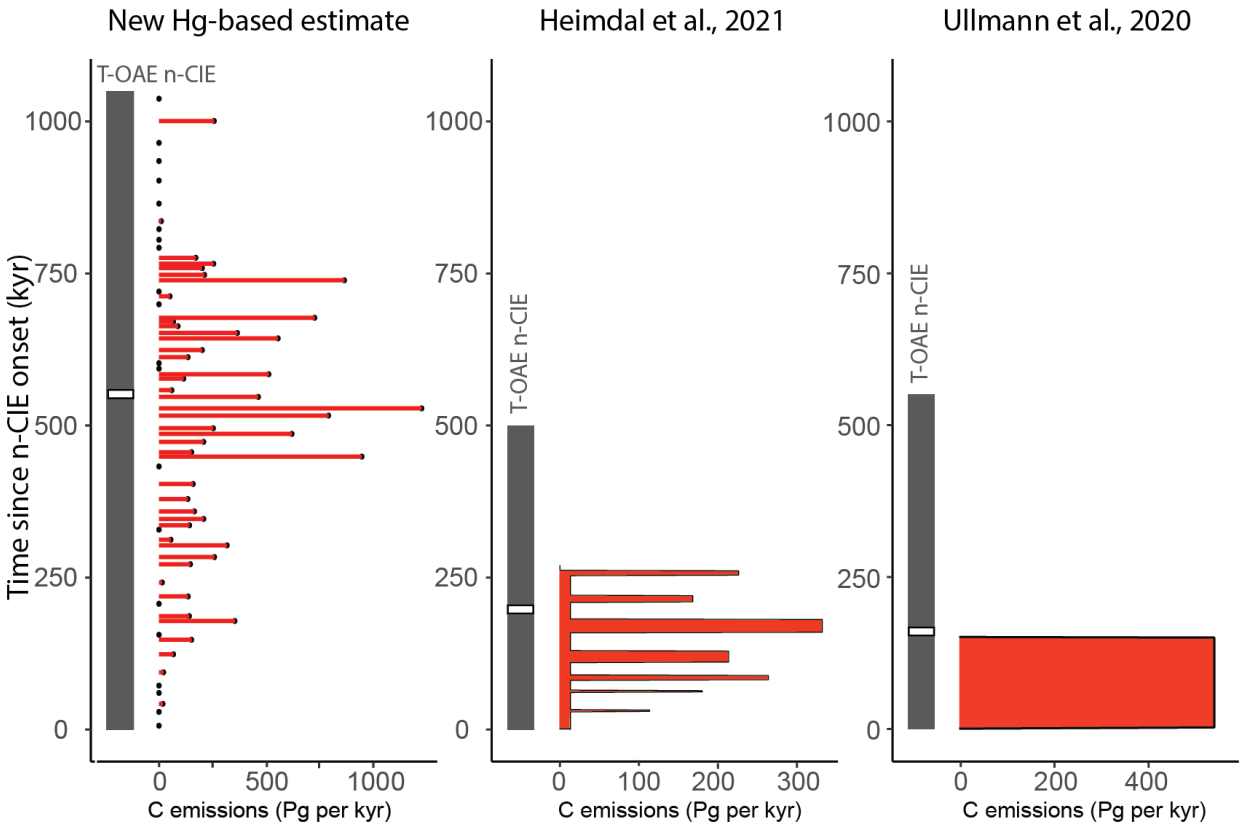

Figure S13: The C-emissions vs time since onset of the T-OAE n-CIE for the Hg-based and each literature model T-OAE C emissions scenario. In all three emissions scenarios, the majority of C is emitted during approximately the first half of the CIE, prior to the nadir (indicated as a white box on the grey bar). In the case of our new record (left panel), the first 550 kyr contain 60% of the total C emitted, whereas in the model scenarios most (80% in Heimdal et al.; 100% in Ullmann et al.) of the C is released during the falling limb of the CIE.

The n-CIE as represented in our new record is substantially longer than in the two modelled scenarios. See SI S3 (Age Model). Note: the height (thickness) of the red bars in the Hg-based estimates (to indicate summed area = total emissions) is illustrative only – each data point is calculated to represent 1000 years (see S4.1).

S5: Evaluating potential CAMP volcanism at Sinemurian – Pliensbachian boundary:

Here, we briefly evaluate the evidence for CAMP volcanism around the S–P boundary. The main CAMP phase ended at ~200 Ma[70,71] and although CAMP-associated, primarily submarine, volcanism persisted during continental rifting to mid-ocean ridge spreading center development, the ages of these eruptions are poorly constrained[72]. There is no volcanological/geochronological evidence of a major pulse of activity near the Sinemurian–Pliensbachian boundary as required to release enough CO_2 to drive the major (5-Myr duration, 3–4 ‰[13]) S–P n-CIE: the longer the duration of a CIE, the more substantial the carbon cycle imbalance must be[73].

The hypothesis for CAMP volcanism as a driver of the S – P boundary n-CIE is primarily based on Sr isotope composition data which suggest a plateau on top of a generally decreasing trend through the early Jurassic[74]. This trend suggests an increase in continental weathering/runoff during this time interval which is presumably driven by increased precipitation due to a warmer climate (and higher pCO_2). This climate change is a potential consequence of volcanic CO_2 emissions; however, it does not uniquely fingerprint a volcanic driver. Instead, this climate change might have been driven by sea-level or tectonic changes – especially relevant for this time interval which witnessed the ongoing opening of the Atlantic Ocean.

Given that submarine LIP volcanism, such as the known late-stage CAMP activity, tends to only leave regional sedimentary Hg signals[10], we cannot exclude that such activity played a significant role through volcanic carbon emissions while not leaving concomitant record in the Mochras core. However, considering CAMP was emplaced relatively close to the Mochras section (main text Fig. 1), it is conceivable that Hg_R might record these submarine eruptions and therefore it is still useful as evidence for whether enhanced volcanism (both submarine or subaerial) is present during this period. As a result, our new Hg_R record does not support a volcanic driver of the n-CIE. Although we cannot exclude the possibility of submarine volcanism playing a significant role, the especially long duration of the n-CIE is not typical of other known LIP-associated n-CIEs (e.g., T-OAE[38], PETM[75]).

S6: Example code to generate Hg residual for Mochras dataset:

This was written in R (version 4.2.3 “Shortstop Beagle”) using RStudio

```
## Notes: This script fits Hg vs TOC data using robust nonlinear
regression using the R package robustbase. EXAMINE YOUR DATA
FIRST. This assumes that there is NOT a negative relationship
between Hg and TOC (positive slope: constant or decreasing, or
no relationship OK, though result will not be meaningful/will
likely be a flat line in that case). It will also recognize
```

```
outliers. In order for the best-fit curve to represent actual
background, there must be sufficient background (not anomalously
high Hg) data. I use TOC here and throughout but any parameter
can be used (e.g., S, Al).

library(robustbase)
library(ggplot2)
#check dependencies

#setwd as appropriate

#Load data

read.csv("Fendley_Mochras_all.csv",skip=1)->Mochras

#Calculate CaCO3-free values for Hg, TOC

Mochras$Hg_cf<- Mochras$Hg/(1-Mochras$CaCO3_calc/100)
Mochras$TOC_cf<- Mochras$TOC/(1-Mochras$CaCO3_calc/100)

Hg<-as.vector(Mochras$Hg_cf)
TOC<-as.vector(Mochras$TOC_cf)

formulaExp<- Hg ~ (a*tanh(TOC/b) + c) #This is the formula we
expect, with a, b, and c as the parameters to solve for
nonlinfit <- nlrob(formulaExp,lower= c(a=0,b=0.01,c=0), upper
=c(a=900,b=900,c=1000)
,method="MM",data=cbind.data.frame(TOC,Hg))

#if using M then need start=list(a=100,b=10,c=500),start is a
list of starting values note this is not a lower limit. For MM
```

```
need lower and upper limits defined and make sure that the
limits of a and b are larger than maximum Hg and TOC
respectively. Sometimes b=0 does not behave well bc of dividing
by 0 so we set a lower limit of 0.01

## Troubleshooting 1) M vs MM - M is generally 'easier' to
handle but if the relationship is quasi-linear/constant slope it
may not converge because the coefficients are nonunique (this is
the case for Mochras cf data). MM tends to not have this problem
because you have min/max for coefficients (but then must take
care choosing these values). 2)Order data by increasing TOC (x)
concentration and then repeat all steps (this should not matter
but sometimes solves problems with figures)

## Then the results of the regression can be incorporated into
the main dataframe

Mochras$test_weights<-nonlinfit$rweights #These are the weights
for each data point for the robust regression. Outliers will
have lower weights.

Mochras$test_residuals<-nonlinfit$residuals # These are the
residual Hg for each data point (this is what you want in the
end)

Mochras$test_predict<-predict(nonlinfit) # These are the
predicted Hg values for each TOC for each data point (this makes
the best fit curve)

nonlinfit$coefficients #This will show you a, b, and c for the
fit

## For Mochras Hg_cf and TOC_cf the coefficients are a=578.21,
b=181.22, c=48.94

Mochras$HgTOC <- Mochras$Hg/Mochras$TOC
```

```
## Example figures:

ggplot(data=Mochras,aes(TOC_cf,Hg_cf,col=test_weights))+geom_poi
nt()+geom_line(aes(TOC_cf,test_predict),col="blue")+theme_classi
c()+ylab("Hg (ppb)")+xlab("TOC (weight %)")

ggplot(data=Mochras,aes(TOC,HgTOC))+geom_hline(yintercept=10)+ge
om_point()+theme_classic()+ylab("Hg/TOC (ppb/wt %)")+xlab("TOC
(weight %)")

ggplot(data=Mochras,aes(TOC_cf,test_residuals,col=test_weights))
+geom_point()+theme_classic()+ylab("Residual Hg
(ppb)")+xlab("TOC_cf (weight %)")


#Check if the same as in paper (small variability can occur but
should bestable):

ggplot(data=Mochras,aes(test_residuals,Hg_residual))+geom_point(
)+geom_abline(slope=1,intercept=0)


#Plot with time

ggplot(data=Mochras,
aes(Age,test_residuals))+geom_point()+theme_classic()
```

S7: Data Tables:

Two data files: Dataset 1/"New_Hg_data.csv" which contains the new Hg data for this study, and Dataset 2/"Fendley_Mochras_all.csv" which contains the complete Mochras Hg compilation, including calculated Hg_R and Hg emissions. These both are available at: https://doi.org/10.6084/m9.figshare.23301311

References:

1. Percival, L. M. E. *et al.* Globally enhanced mercury deposition during the end-Pliensbachian extinction and Toarcian OAE: A link to the Karoo–Ferrar Large Igneous Province. *Earth and Planetary Science Letters* **428**, 267–280 (2015).
2. Percival, L. M. E. *et al.* Osmium isotope evidence for two pulses of increased continental weathering linked to Early Jurassic volcanism and climate change. *Geology* **44**, 759–762 (2016).
3. Ruhl, M. *et al.* Reduced plate motion controlled timing of Early Jurassic Karoo-Ferrar large igneous province volcanism. *Science Advances* **8**, eabo0866 (2022).
4. Shen, J. *et al.* Sedimentary host phases of mercury (Hg) and implications for use of Hg as a volcanic proxy. *Earth and Planetary Science Letters* **543**, 116333 (2020).
5. Gębka, K., Saniewska, D. & Bełdowska, M. Mobility of mercury in soil and its transport into the sea. *Environ Sci Pollut Res* **27**, 8492–8506 (2020).
6. Ravichandran, M. Interactions between mercury and dissolved organic matter—a review. *Chemosphere* **55**, 319–331 (2004).
7. Grasby, S. E., Them, T. R., Chen, Z., Yin, R. & Ardakani, O. H. Mercury as a proxy for volcanic emissions in the geologic record. *Earth-Science Reviews* **196**, 102880 (2019).
8. Sanei, H., Grasby, S. E. & Beauchamp, B. Latest Permian mercury anomalies. *Geology* **40**, 63–66 (2012).
9. Wilman, B., Saniewska, D., Pyta, H., Wysiecki, D. & Bełdowska, M. Mercury fractionation - Problems in method application. *Marine Pollution Bulletin* **187**, 114560 (2023).
10. Percival, L. M. E. *et al.* Does large igneous province volcanism always perturb the mercury cycle? Comparing the records of Oceanic Anoxic Event 2 and the end-Cretaceous to other Mesozoic events. *American Journal of Science* **318**, 799–860 (2018).
11. Meyer, K. W. *et al.* Biogenic carbonate mercury and marine temperature records reveal global influence of Late Cretaceous Deccan Traps. *Nat Commun* **10**, 5356 (2019).

12. Weedon, G. P. & Jenkyns, H. C. Regular and irregular climatic cycles and the Belemnite Marls (Pliensbachian, Lower Jurassic, Wessex Basin). *Journal of the Geological Society* **147**, 915 LP – 918 (1990).
13. Storm, M. S. *et al.* Orbital pacing and secular evolution of the Early Jurassic carbon cycle. *Proceedings of the National Academy of Sciences* **117**, 3974–3982 (2020).
14. Xu, W. *et al.* Evolution of the Toarcian (Early Jurassic) carbon-cycle and global climatic controls on local sedimentary processes (Cardigan Bay Basin, UK). *Earth and Planetary Science Letters* **484**, 396–411 (2018).
15. Nasr, M. & Arp, P. A. Mercury and Organic Matter Concentrations in Lake and Stream Sediments in relation to One Another and to Atmospheric Mercury Deposition and Climate Variations across Canada. *Journal of Chemistry* **2017**, 8949502 (2017).
16. Schuster, P. F. *et al.* Permafrost Stores a Globally Significant Amount of Mercury. *Geophysical Research Letters* **45**, 1463–1471 (2018).
17. Ballabio, C. *et al.* A spatial assessment of mercury content in the European Union topsoil. *Science of The Total Environment* **769**, 144755 (2021).
18. Shen, J. *et al.* Evidence for a prolonged Permian–Triassic extinction interval from global marine mercury records. *Nature Communications* **10**, 1563 (2019).
19. Jin, H., Liebezeit, G. & Ziehe, D. Distribution of Total Mercury in Surface Sediments of the Western Jade Bay, Lower Saxonian Wadden Sea, Southern North Sea. *Bull Environ Contam Toxicol* **88**, 597–604 (2012).
20. Maechler, M. *et al.* R Package 'robustbase': Basic Robust Statistics. (2021).
21. Maher, K. & Chamberlain, C. P. Hydrologic Regulation of Chemical Weathering and the Geologic Carbon Cycle. *Science* **343**, 1502–1504 (2014).

22. Kennedy, M. J., Löhr, S. C., Fraser, S. A. & Baruch, E. T. Direct evidence for organic carbon preservation as clay-organic nanocomposites in a Devonian black shale; from deposition to diagenesis. *Earth and Planetary Science Letters* **388**, 59–70 (2014).
23. Ullmann, C. V., Szùcs, D., Jiang, M., Hudson, A. J. L. & Hesselbo, S. P. Geochemistry of macrofossil, bulk rock and secondary calcite in the Early Jurassic strata of the Llanbedr (Mochras Farm) drill core, Cardigan Bay Basin, Wales, UK. *Journal of the Geological Society* **179**, jgs2021-018 (2022).
24. Copestake, P. & Johnson, B. Lower Jurassic Foraminifera from the Llanbedr (Mochras Farm) Borehole, North Wales, UK. *Monographs of the Palaeontographical Society* **167**, 1–403 (2013).
25. Ivimey-Cook, H. C. Stratigraphical Palaeontology of the Lower Jurassic of the Llanbedr (Mochras Farm) Borehole. in *The Llanbedr (Mochras Farm) Borehole* (ed. Woodland, A. W.) vol. Institute of Geological Sciences Report No. 71/18 87–92 (1971).
26. Frieling, J. *et al.* Effects of redox variability and early diagenesis on marine sedimentary Hg records. *Geochimica et Cosmochimica Acta* (2023) doi:10.1016/j.gca.2023.04.015.
27. Charbonnier, G., Adatte, T., Föllmi, K. B. & Suan, G. Effect of Intense Weathering and Postdepositional Degradation of Organic Matter on Hg/TOC Proxy in Organic-rich Sediments and its Implicationsfor Deep-Time Investigations. *Geochemistry, Geophysics, Geosystems* **21**, 270 (2020).
28. Shen, J., Algeo, T. J. & Feng, Q. Mercury isotope evidence for a non-volcanic origin of Hg spikes at the Ordovician-Silurian boundary, South China. *Earth and Planetary Science Letters* **594**, 117705 (2022).
29. Wang, Y. *et al.* The influence of Late Ordovician volcanism on the marine environment based on high-resolution mercury data from South China. *GSA Bulletin* **135**, 787–798 (2023).
30. Mercone, D., Thomson, J., Croudace, I. W. & Troelstra, S. R. A coupled natural immobilisation mechanism for mercury and selenium in deep-sea sediments. *Geochimica et Cosmochimica Acta* **63**, 1481–1488 (1999).

31. Them, T. R. *et al.* Terrestrial sources as the primary delivery mechanism of mercury to the oceans across the Toarcian Oceanic Anoxic Event (Early Jurassic). *Earth and Planetary Science Letters* **507**, 62–72 (2019).
32. Amos, H. M. *et al.* Global biogeochemical implications of mercury discharges from rivers and sediment burial. *Environmental Science & Technology* **48**, 9514–9522 (2014).
33. Amos, H. M. *et al.* Observational and Modeling Constraints on Global Anthropogenic Enrichment of Mercury. *Environmental Science & Technology* **49**, 4036–4047 (2015).
34. Selin, N. E. Global Biogeochemical Cycling of Mercury: A Review. *Annual Review of Environment and Resources* **34**, 43–63 (2009).
35. Friedli, H. R., Arellano, A. F., Cinnirella, S. & Pirrone, N. Initial Estimates of Mercury Emissions to the Atmosphere from Global Biomass Burning. *Environmental Science & Technology* **43**, 3507–3513 (2009).
36. Hollaar, T. P. *et al.* Wildfire activity enhanced during phases of maximum orbital eccentricity and precessional forcing in the Early Jurassic. *Commun Earth Environ* **2**, 1–12 (2021).
37. Al-Suwaidi, A. H. *et al.* New age constraints on the Lower Jurassic Pliensbachian–Toarcian Boundary at Chacay Melehue (Neuquén Basin, Argentina). *Scientific Reports* **12**, 4975 (2022).
38. Hesselbo, S. P., Ogg, J. G., Ruhl, M., Hinnov, L. A. & Huang, C. J. Chapter 26 - The Jurassic Period. in *Geologic Time Scale 2020* (eds. Gradstein, F. M., Ogg, J. G., Schmitz, M. D. & Ogg, J. G.) vol. 2 955–1021 (Elsevier, 2020).
39. Kemp, D. B., Suan, G., Fantasia, A., Jin, S. & Chen, W. Global organic carbon burial during the Toarcian oceanic anoxic event: Patterns and controls. *Earth-Science Reviews* **231**, 104086 (2022).
40. Suan, G., Mattioli, E., Pittet, B., Mailliot, S. & Lécuyer, C. Evidence for major environmental perturbation prior to and during the Toarcian (Early Jurassic) oceanic anoxic event from the Lusitanian Basin, Portugal. *Paleoceanography* **23**, (2008).

41. Huang, C. & Hesselbo, S. P. Pacing of the Toarcian Oceanic Anoxic Event (Early Jurassic) from astronomical correlation of marine sections. *Gondwana Research* **25**, 1348–1356 (2014).
42. Boulila, S., Galbrun, B., Sadki, D., Gardin, S. & Bartolini, A. Constraints on the duration of the early Toarcian T-OAE and evidence for carbon-reservoir change from the High Atlas (Morocco). *Global and Planetary Change* **175**, 113–128 (2019).
43. Fendley, I. M. *et al.* Constraints on the volume and rate of Deccan Traps flood basalt eruptions using a combination of high-resolution terrestrial mercury records and geochemical box models. *Earth and Planetary Science Letters* **524**, 115721 (2019).
44. Goulet, R. R. *et al.* Mercury transformations and fluxes in sediments of a riverine wetland. *Geochimica et Cosmochimica Acta* **71**, 3393–3406 (2007).
45. Amos, H. M., Jacob, D. J., Streets, D. G. & Sunderland, E. M. Legacy impacts of all-time anthropogenic emissions on the global mercury cycle. *Global Biogeochemical Cycles* **27**, 410–421 (2013).
46. Siegel, B. Z. & Siegel, S. M. Hawaiian volcanoes and the biogeology of mercury. in *Volcanism in Hawaii* vol. U.S. Geological Survey Professional Paper 1350 827–839 (1987).
47. Bagnato, E. *et al.* Degassing of gaseous (elemental and reactive) and particulate mercury from Mount Etna volcano (Southern Italy). *Atmospheric Environment* **41**, 7377–7388 (2007).
48. Shinohara, H., Aiuppa, A., Giudice, G., Gurrieri, S. & Liuzzo, M. Variation of H2O/CO2 and CO2/SO2 ratios of volcanic gases discharged by continuous degassing of Mount Etna volcano, Italy. *Journal of Geophysical Research: Solid Earth* **113**, (2008).
49. Bagnato, E. *et al.* First simultaneous mercury and major volatiles characterization of atmospheric hydrothermal emissions at the Pisciarelli's fumarolic system (Campi Flegrei, Italy). *Journal of Volcanology and Geothermal Research* **406**, 107074 (2020).

50. Cabassi, J. *et al.* Flux measurements of gaseous elemental mercury (GEM) from the geothermal area of “Le Biancane” natural park (Monterotondo Marittimo, Grosseto, Italy): Biogeochemical processes controlling GEM emission. *Journal of Geochemical Exploration* **228**, 106824 (2021).
51. Witt, M. L. I. *et al.* Mercury and halogen emissions from Masaya and Telica volcanoes, Nicaragua. *Journal of Geophysical Research: Solid Earth* **113**, B06203 (2008).
52. Bagnato, E. *et al.* Hg and CO2 emissions from soil diffuse degassing and fumaroles at Furnas Volcano (São Miguel Island, Azores): Gas flux and thermal energy output. *Journal of Geochemical Exploration* **190**, 39–57 (2018).
53. Zerizghi, T., Guo, Q., Zhao, C. & Okoli, C. P. Sulfur, lead, and mercury characteristics in South Africa coals and emissions from the coal-fired power plants. *Environ Earth Sci* **81**, 116 (2022).
54. O’Keefe, J. M. K. *et al.* CO2, CO, and Hg emissions from the Truman Shepherd and Ruth Mullins coal fires, eastern Kentucky, USA. *Science of The Total Environment* **408**, 1628–1633 (2010).
55. Engle, M. A. *et al.* Gas emissions, minerals, and tars associated with three coal fires, Powder River Basin, USA. *Science of The Total Environment* **420**, 146–159 (2012).
56. Hong, X. *et al.* Mercury emissions from dynamic monitoring holes of underground coal fires in the Wuda Coalfield, Inner Mongolia, China. *International Journal of Coal Geology* **181**, 78–86 (2017).
57. Heimdal, T. H., Goddéris, Y., Jones, M. T. & Svensen, H. H. Assessing the importance of thermogenic degassing from the Karoo Large Igneous Province (LIP) in driving Toarcian carbon cycle perturbations. *Nat Commun* **12**, 6221 (2021).
58. Ullmann, C. V. *et al.* Warm afterglow from the Toarcian Oceanic Anoxic Event drives the success of deep-adapted brachiopods. *Sci Rep* **10**, 6549 (2020).
59. White, R. S. Mantle plume origin for the Karoo and Ventersdorp flood basalts, South Africa. *South African Journal of Geology* **100**, 271–282 (1997).

60. Svensen, H. H. *et al.* Understanding thermogenic degassing in large igneous provinces: Inferences from the geological and statistical characteristics of breccia pipes in the western parts of the Karoo Basin. in *Mass Extinctions, Volcanism, and Impacts: New Developments* (eds. Adatte, T., Bond, D. P. G. & Keller, G.) vol. 544 0 (Geological Society of America, 2020).
61. Black, B. A., Karlstrom, L. & Mather, T. A. The life cycle of large igneous provinces. *Nat Rev Earth Environ* **2**, 840–857 (2021).
62. Penman, D. E., Caves Rugenstein, J. K., Ibarra, D. E. & Winnick, M. J. Silicate weathering as a feedback and forcing in Earth's climate and carbon cycle. *Earth-Science Reviews* **209**, 103298 (2020).
63. Gómez, J. J., Comas-Rengifo, M. J. & Goy, A. Palaeoclimatic oscillations in the Pliensbachian (early Jurassic) of the Asturian Basin (northern Spain). *Climate of the Past* **12**, 1199–1214 (2016).
64. Price, G. D., Baker, S. J., VanDeVelde, J. & Clémence, M.-E. High-resolution carbon cycle and seawater temperature evolution during the Early Jurassic (Sinemurian-Early Pliensbachian). *Geochemistry, Geophysics, Geosystems* **17**, 3917–3928 (2016).
65. Rosales, I., Quesada, S. & Robles, S. Paleotemperature variations of Early Jurassic seawater recorded in geochemical trends of belemnites from the Basque–Cantabrian basin, northern Spain. *Palaeogeography, Palaeoclimatology, Palaeoecology* **203**, 253–275 (2004).
66. Müller, T. *et al.* Ocean acidification during the early Toarcian extinction event: Evidence from boron isotopes in brachiopods. *Geology* **48**, 1184–1188 (2020).
67. Anderson, T. F. & Arthur, M. A. Stable Isotopes of Oxygen and Carbon and their Application to Sedimentologic and Paleoenvironmental Problems. in *Stable Isotopes in Sedimentary Geology* (eds. Arthur, M. A., Anderson, T. F., Kaplan, I. R., Veizer, J. & Land, L. S.) vol. 10 0 (SEPM Society for Sedimentary Geology, 1983).
68. DeVries, T. The ocean carbon cycle. *Annual Review of Environment and Resources* **47**, 317–341 (2022).

69. Lauvset, S. K. *et al.* An updated version of the global interior ocean biogeochemical data product, GLODAPv2.2021. *Earth System Science Data* **13**, 5565–5589 (2021).
70. Jiang, Q., Jourdan, F., Olierook, H. K. H. & Merle, R. E. An appraisal of the ages of Phanerozoic large igneous provinces. *Earth-Science Reviews* **237**, 104314 (2023).
71. Marzoli, A. *et al.* The Central Atlantic magmatic province (CAMP): A review. in *The Late Triassic World* (ed. Tanner, L. H.) vol. 46 91–125 (Springer, 2018).
72. Lang, G., ten Brink, U. S., Hutchinson, D. R., Mountain, G. S. & Schattner, U. The Role of Premagmatic Rifting in Shaping a Volcanic Continental Margin: An Example from the Eastern North American Margin. *Journal of Geophysical Research: Solid Earth* **125**, e2020JB019576 (2020).
73. Vervoort, P., Adloff, M., Greene, S. E. & Turner, S. K. Negative carbon isotope excursions: an interpretive framework. *Environ. Res. Lett.* **14**, 085014 (2019).
74. Ruhl, M. *et al.* Astronomical constraints on the duration of the Early Jurassic Pliensbachian Stage and global climatic fluctuations. *Earth and Planetary Science Letters* **455**, 149–165 (2016).
75. Kirtland Turner, S. & Ridgwell, A. Development of a novel empirical framework for interpreting geological carbon isotope excursions, with implications for the rate of carbon injection across the PETM. *Earth and Planetary Science Letters* **435**, 1–13 (2016).